

**1 Local wind regime induced by giant linear dunes:
2 comparison of ERA5-Land reanalysis with surface
3 measurements**

**4 Cyril Gadal · Pauline Delorme ·
5 Clément Narteau · Giles F.S. Wiggs ·
6 Matthew Baddock · Joanna M. Nield ·
7 Philippe Claudin**

8
9 Received: DD Month YEAR / Accepted: DD Month YEAR

10 Abstract

11 Emergence and growth of sand dunes results from the dynamic interaction
12 between topography, wind flow and sediment transport. While feedbacks be-
13 tween these variables are well studied at the scale of a single and relatively
14 small dune, the average effect of a periodic large-scale dune pattern on at-
15 mospheric flows remains poorly constrained, due to a pressing lack of data
16 in major sand seas. Here, we compare local measurements of surface winds
17 to the predictions of the ERA5-Land climate reanalysis at four locations in
18 Namibia, both within and outside the giant linear dune field of the Namib
19 Sand Sea. In the desert plains to the north of the sand sea, observations and
20 predictions agree well. This is also the case in the interdune areas of the sand
21 sea during the day. During the night, however, an additional wind component
22 aligned with the giant dune orientation is measured, in contrast to the easterly

C. Gadal

Institut de Mécanique des Fluides de Toulouse, Université de Toulouse Paul Sabatier, CNRS,
Toulouse INP-ENSEEIHT, Toulouse, France. E-mail: cyril.gadal@imft.fr

P. Delorme

Energy and Environment Institute, University of Hull, Hull, UK.

C. Narteau

Institut de Physique du Globe de Paris, Université de Paris, CNRS, Paris, France.

G. Wiggs

School of Geography and the Environment, University of Oxford, Oxford, UK.

M.C. Baddock

Geography and Environment, Loughborough University, Loughborough, UK.

J.M. Nield

School of Geography and Environmental Science, University of Southampton, Southampton,
UK.

P. Claudin

Physique et Mécanique des Milieux Hétérogènes, CNRS, ESPCI Paris, PSL Research Uni-
versity, Université de Paris, Sorbonne Université, Paris, France.

wind predicted by the ERA5-Land reanalysis. For the given dune orientation and measured wind regime, we link the observed wind deviation (over 50°) to the daily cycle of the turbulent atmospheric boundary layer. During the night, a shallow boundary layer induces a flow confinement above the giant dunes, resulting in large flow deviations, especially for the slower easterly winds. During the day, the feedback of the giant dunes on the atmospheric flow is much weaker due to the thicker boundary layer and higher wind speeds. Finally, we propose that the confinement mechanism and the associated wind deflections induced by giant dunes could explain the development of smaller-scale secondary dunes, which elongate obliquely in the interdune areas of the primary dune pattern.

Keywords Atmospheric boundary layer · Sand dunes · Flow over hills

35 1 Introduction

36 The description of turbulent flows over complex topography is relevant for
37 a large variety of different environmental systems (Sherman 1978; Walmsley
38 et al. 1982; Baines 1995; Wood 2000; Venditti et al. 2013; Finnigan et al.
39 2020). For example, the flow over hills is of primary interest for wind power,
40 meteorological and air pollution phenomena (Taylor et al. 1987). The proper-
41 ties of these flows are also key to the understanding of geophysical phenom-
42 ena, including the formation of wind-driven waves on the ocean surface (Sulli-
43 van and McWilliams 2010), dissolution bedforms (Claudin et al. 2017; Guérin
44 et al. 2020), or sedimentary ripples and dunes (Bagnold 1941; Charru et al.
45 2013; Courrech du Pont 2015). Importantly, the troposphere presents a vertical
46 structure, with a lower convective boundary layer, of typical kilometer-scale
47 thickness, capped by a stably stratified region (Stull 1988). The largest topo-
48 graphic obstacles, such as mountains, can therefore interact with this upper
49 region and lead to internal wave generation or significant wind disturbances,
50 such as lee-side downslope winds (Durran 1990).

51 Compared to hills and mountains, aeolian sand dunes offer idealized ele-
52 vation profiles for the study of atmospheric turbulent flow over topographies,
53 due to their smooth shape, free of canopies. Besides, dunes provide a rather
54 wide range of scales, from decameters to kilometers, and very often come in
55 a fairly regular pattern, which further simplifies the flow structure analysis.
56 Past studies have highlighted two important topographic feedbacks on the
57 wind flow close to the dune/hill surface. First is the effect on wind speed, with
58 documented flow acceleration on upwind slopes (Weaver and Wiggs 2011) and
59 deceleration on downwind slopes (Baddock et al. 2007), where the speed-up
60 factor is essentially proportional to the obstacle aspect ratio (Jackson and Hunt
61 1975). Under multidirectional wind regimes with frequent wind reversals, this
62 speed-up effect induces large differences in the amplitude and orientation of
63 the resultant sediment transport between flat sand beds and the dune crests
64 (Zhang et al. 2014; Rozier et al. 2019; Gao et al. 2021). In addition, the po-
65 sition of maximum velocity is typically shifted upwind of the obstacle crest
66 (Jackson and Hunt 1975; Claudin et al. 2013). This behaviour has been the-
67oretically predicted by means of asymptotic analysis of a neutrally stratified
68 boundary-layer flow over an obstacle of vanishing aspect ratio (Jackson and
69 Hunt 1975; Mason and Sykes 1979; Sykes 1980; Hunt et al. 1988; Belcher and
70 Hunt 1998; Kroy et al. 2002). Experiments in flumes (Zilker et al. 1977; Zilker
71 and Hanratty 1979; Frederick and Hanratty 1988; Poggi et al. 2007; Bristow
72 et al. 2022), in wind tunnels (Gong and Ibbetson 1989; Finnigan et al. 1990;
73 Gong et al. 1996) and in field conditions at all scales (Taylor and Teunissen
74 1987; Claudin et al. 2013; Fernando et al. 2019; Lü et al. 2021), have also
75 documented this effect. Interestingly, a similar behaviour exists for the pres-
76 sure perturbation, but with a slight downwind shift for the pressure minimum
77 (Claudin et al. 2021).

78 The second effect, much less studied, is the flow deflection that occurs when
79 the incident wind direction is not perpendicular to the ridge crest. While pre-

dicted to be small (less than 10°) in the linear regime valid for shallow topography (Gadal et al. 2019), significant flow steering has been reported in the field on the downwind side of steep enough obstacles, such as well-developed sand dunes (Tsoar and Yaalon 1983; Sweet and Kocurek 1990; Walker and Nickling 2002; Smith et al. 2017) and in particular coastal foredunes (e.g. Hunter et al. 1983; Rasmussen 1989; Walker et al. 2006, 2009; Hesp et al. 2015; Walker et al. 2017; de Winter et al. 2020), mountain ranges (Kim et al. 2000; Lewis et al. 2008; Fernando et al. 2019), and valley topographies (Wiggs et al. 2002; Garvey et al. 2005).

Wind measurements over sand dunes have been mainly performed over small bedforms, typically a few meters high (corresponding to several tens of meters long) (e.g. Mulligan 1988; Hesp et al. 1989; Lancaster et al. 1996; McKenna Neuman et al. 1997; Sauermann et al. 2003; Andreotti et al. 2002; Walker and Nickling 2002; Weaver and Wiggs 2011). For practical reasons, fewer studies have performed similar measurements on giant dunes (Havholm and Kocurek 1988), with kilometer-scale wavelengths and heights of tens of meters. However, such large dunes provide a choice configuration for the study of turbulent flows over a complex topography. First, one expects larger wind disturbances for larger obstacles. Secondly, their large size can make them interact with the vertical structure of the atmosphere (Andreotti et al. 2009). Third, they usually form large patterns in sand seas and thus behave as rather clean periodic perturbations, in contrast with isolated dunes. Finally, because the morphodynamics of aeolian bedforms is strongly dependent on the local wind regime (Livingstone and Warren 2019), one can expect to see the consequences of windflow disturbance by large dunes on neighbouring small dunes (Brookfield 1977; Ewing et al. 2006). A similar effect is observed on the properties of impact ripple patterns due to the presence of dunes (Howard 1977; Hood et al. 2021).

Atmospheric flows have been much studied at the desert-scale with climate reanalyses based on global atmospheric models (Blumberg and Greeley 1996; Livingstone et al. 2010; Ashkenazy et al. 2012; Jolivet et al. 2021; Hu et al. 2021; Gunn et al. 2021), such as ERA-40, ERA-Interim or ERA5 (Uppala et al. 2005; Dee et al. 2011; Hersbach et al. 2020). However, the spatial resolution of these reanalyses (tens of kilometers) implies average quantities that do not resolve the smaller scales of interest, which range from individual dunes to small mountains (Livingstone et al. 2010). Recently, the release of ERA5-Land has partly resolved this limitation by providing up to 70 years of hourly wind predictions at a 9 km spatial resolution (Muñoz-Sabater et al. 2021). However, its validity remains to be studied, especially in remote desert areas where assimilation of measured data is very low.

In this work, we compare local wind speeds and directions measured by meteorological stations at four different locations inside and north of the giant linear dune field of the Namib sand sea to the regional predictions of the ERA5-Land climate reanalysis. Where the meteorological stations are surrounded by a relatively flat environment, we show that local measurements and regional predictions agree well. The agreement is also good in the interdune areas of

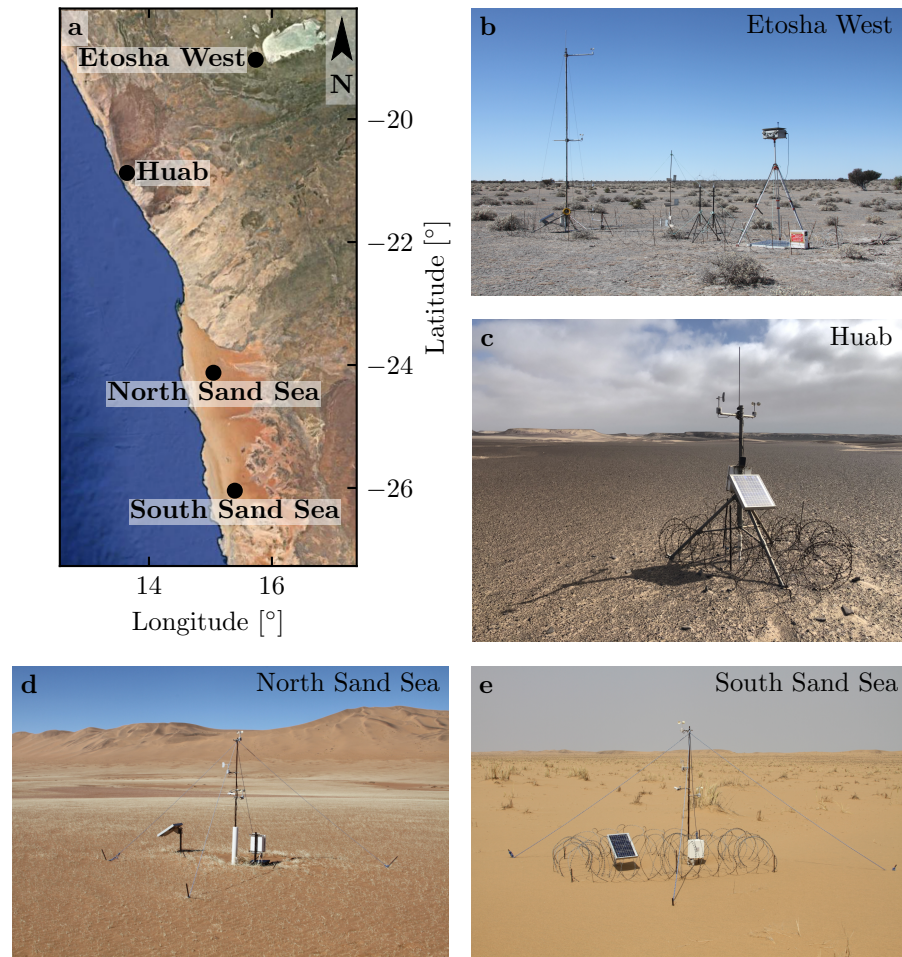


Fig. 1 Studied field sites. **a:** Location of the different sites in Namibia. **b–e:** Photographs of the meteorological stations.

the sand sea, except for some weak winds blowing at night, which exhibit an additional component aligned with the giant dune orientation. These winds are not predicted by the ERA5-Land reanalysis (section 2). Further, we are able to link the magnitude of these differences to the circadian cycle of the atmospheric boundary layer (section 3). Finally, we draw implications for the wind disturbances on smaller-scale dunes (section 4), suggesting a possible origin for crossing dunes, a distinctive secondary dune form observed in the Namib and other sand seas.

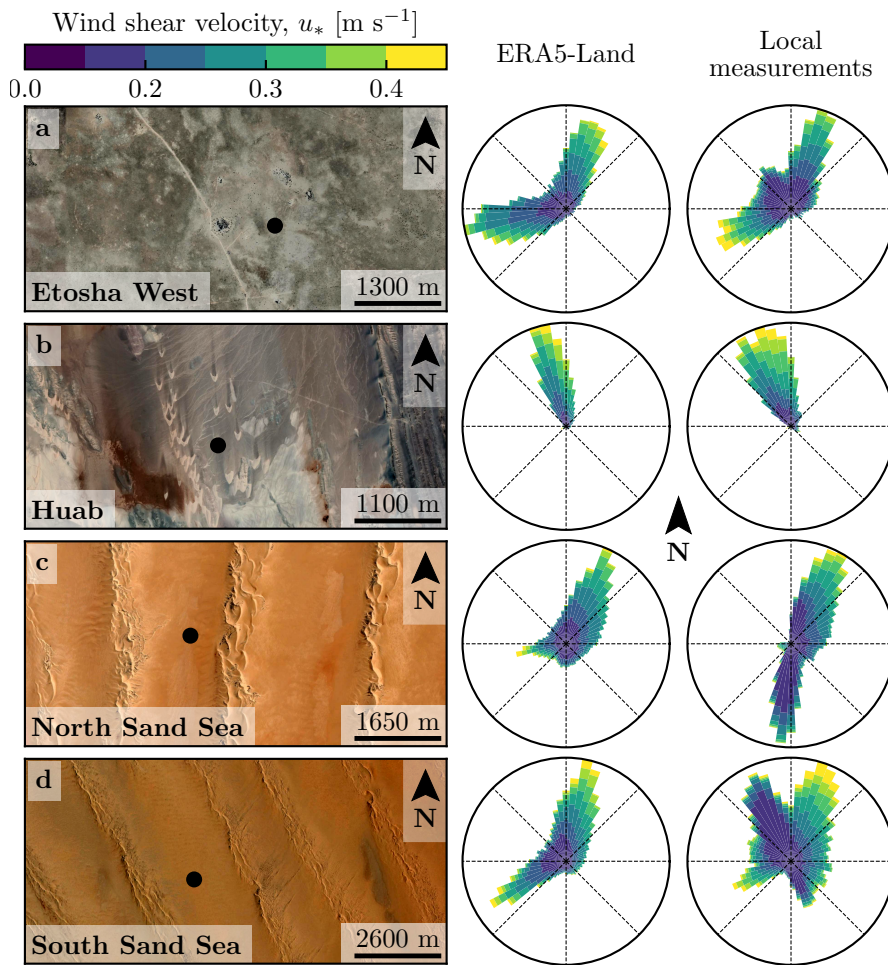


Fig. 2 Wind data used in this study. Satellite images of the different environments (Google-Earth, Maxar Technologies, CNES/Airbus) are shown on the left. The black dots show the location of the wind measurements stations. On the right of the photos, the corresponding wind roses representing the data from the ERA5-Land climate reanalysis and the local wind stations are displayed. Note: the graphical convention for the wind roses is that the bars show the direction towards which the wind blows (see color bar for velocity scale).

134 2 Wind regimes across the Namib Sand Sea

135 We measured the wind regime at four different locations in Namibia, represen-
 136 tative of various arid environments across the Namib desert (Fig. 1, Fig. 2).
 137 The Etosha West station was located at the Adamax waterhole to the west
 138 of Etosha Pan in northern Namibia, in a sparsely vegetated area. The Huab
 139 station was near the coast on a hyper-arid flat gravel plain lying north of
 140 the ephemeral Huab river. Here, barchan dunes up to a few meters in height

141 develop from the sediment blowing out of the river valley (Nield et al. 2017;
142 Hesp and Hastings 1998). These two stations were both located in relatively
143 flat environments. In contrast, the North Sand Sea and South Sand Sea sta-
144 tions were located in the interdunes between linear dunes with kilometer-scale
145 wavelengths, hectometer-scale heights and superimposed patterns. In this sec-
146 tion, we describe and compare winds from local measurements and climate
147 reanalysis predictions.

148 2.1 Wind and elevation data

149 At each meteorological station (Fig. 1), wind speed and direction were sampled
150 every 10 minutes using cup anemometers (Vector Instruments A100-LK) and
151 wind vanes (Vector Instruments W200-P) at a single height, which was between
152 2 m and 3 m depending on the station. The available period of measurements at
153 each station ranged from 1 to 5 discontinuous years distributed between 2012
154 and 2020 (Online Resource Fig. S1). We checked that at least one complete
155 seasonal cycle was available for each station. Regional winds were extracted
156 at the same locations and periods from the ERA5-Land dataset, which is a
157 replay at a smaller spatial resolution of ERA5, the latest climate reanalysis
158 from the ECMWF (Hersbach et al. 2020; Muñoz-Sabater et al. 2021). This
159 dataset provided hourly predictions of the 10-m wind velocity and direction
160 at a spatial resolution of $0.1^\circ \times 0.1^\circ$ ($\simeq 9$ km in Namibia).

161 To enable direct comparison, the local wind measurements were averaged
162 into 1-hr bins centered on the temporal scale of the ERA5-Land estimates
163 (Online Resource Fig. S2). As the wind velocities of both datasets were pro-
164 vided at different heights, we converted them into shear velocities u_* (Online
165 Resource section 1), characteristic of the turbulent wind profile. Wind roses
166 in Fig. 2 show the resulting wind data.

167 Dune properties were computed using autocorrelation on the 30-m Digital
168 Elevation Models (DEMs) of the shuttle radar topography mission (Farr et al.
169 2007). For the North and South Sand Sea stations, we obtain, respectively,
170 orientations of 85° and 125° with respect to the North, wavelengths of 2.6 km
171 and 2.3 km and amplitudes (or half-heights) of 45 m and 20 m (Online Resource
172 Fig. S4 for more details). This agrees with direct measurements made on site.

173 2.2 Comparison of local and regional winds

174 The measured and predicted wind regimes are shown in Fig. 2. In the Namib,
175 the regional wind patterns are essentially controlled by the sea breeze, result-
176 ing in strong northward components (sometimes slightly deviated by the large
177 scale topography) present in all regional wind roses (Lancaster 1985). These
178 daytime winds are dominant during the period October-March (Fig. 3f and
179 Online Resource Fig. 4f). During April-September, an additional (and often
180 nocturnal) easterly component can also be recorded, induced by the combina-
181 tion of katabatic winds forming in the mountains, and infrequent ‘berg’ winds,

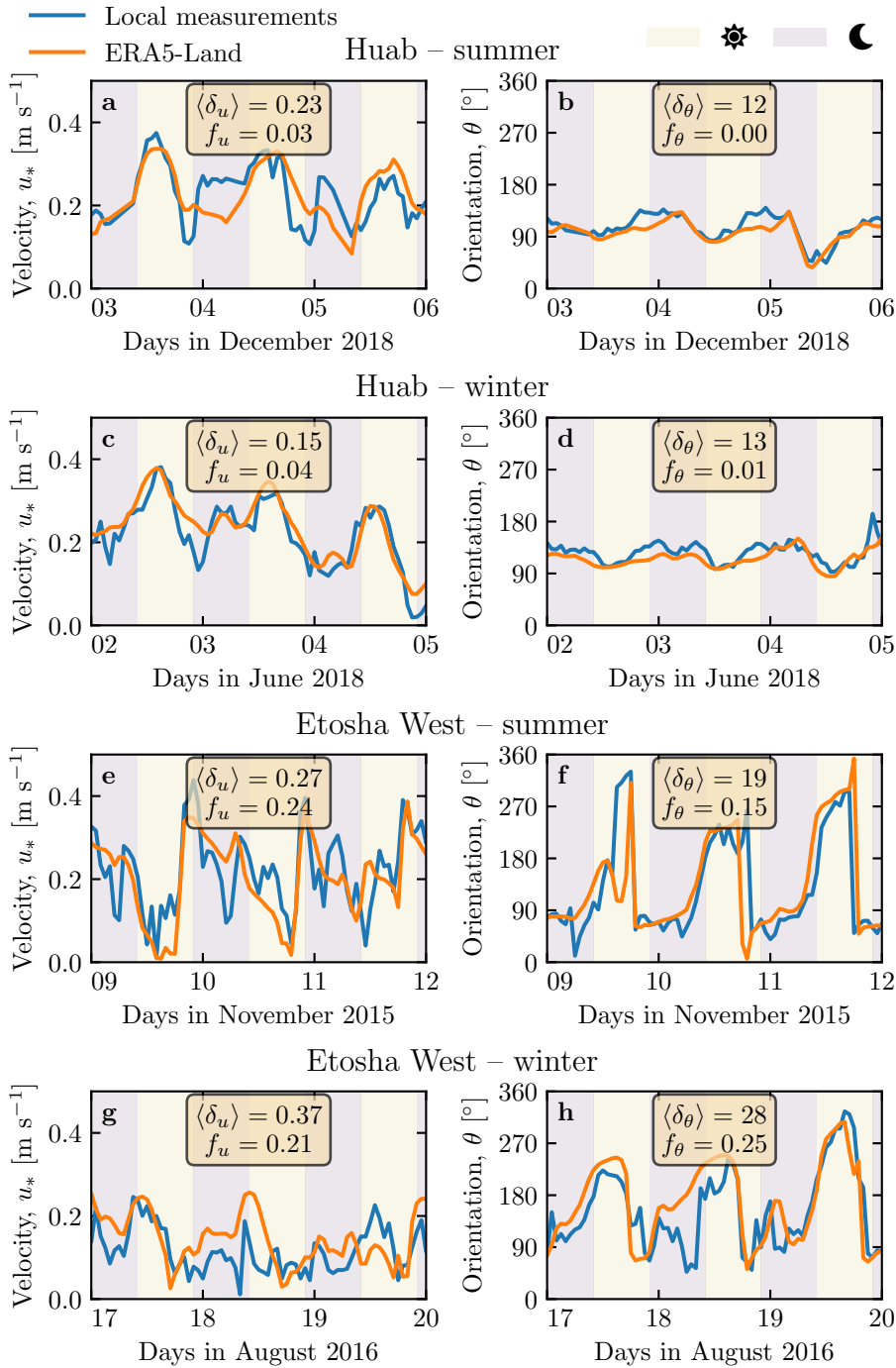


Fig. 3 Temporal comparison between the wind data coming from the ERA5-Land climate reanalysis (orange lines) and from the local measurements (blue lines). Coloured swatches indicate day (between 10.00 UTC and 22.00 UTC) and night (before 10.00 UTC or after 22.00 UTC). Numbers in legends indicate the average flow deflection δ_θ and relative wind modulation δ_u over the displayed period (see section 3.2 for their definitions), as well as the percentage f_θ and f_u of occurrence of extreme events ($\delta_\theta > 50^\circ$, $|\delta_u| > 0.6$). **a–b:** Huab station in summer. **b–c:** Huab station in winter. **d–e:** Etosha West station in summer. **f–g:** Etosha West station in winter. Time series of the two other stations are shown in Fig. 5.

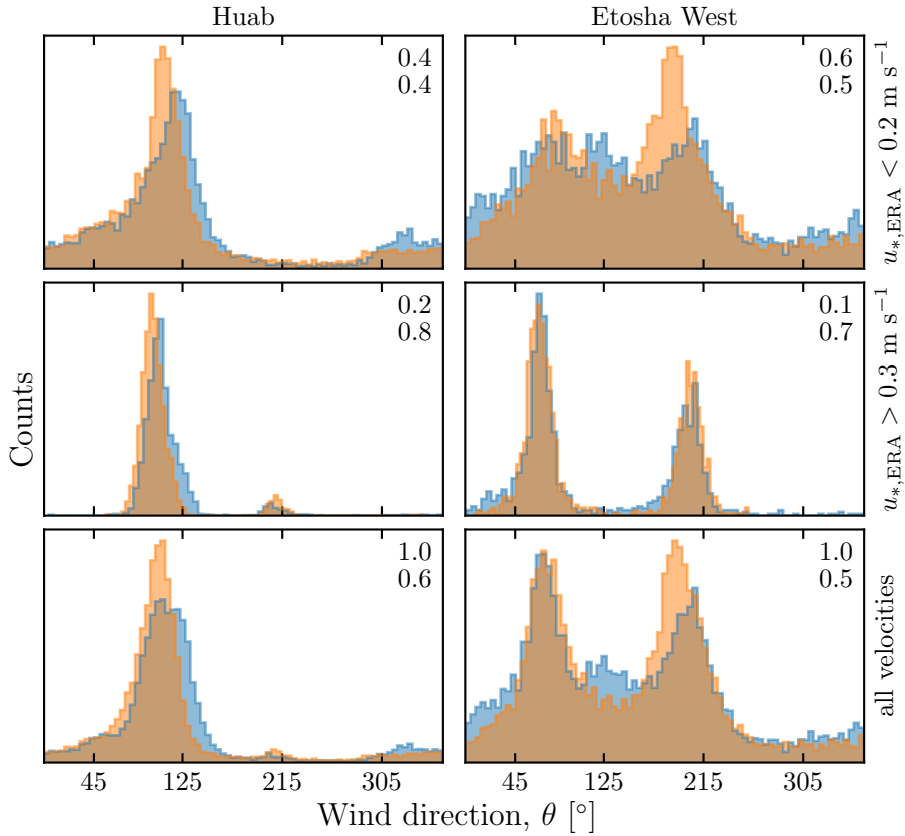


Fig. 4 Distributions of wind direction at Huab and Etosha West stations for the ERA5-Land climate reanalysis (orange) and the local measurements (blue). In each subplot, both distributions are plotted from the same time steps, selected for different ranges of the wind wind velocity (rows) in the ERA5-Land dataset. The numbers at the upper right corners give the percentage of time steps selected in each sub-range (top), as well as the percentage of them corresponding to the day – defined between 10.00 UTC and 22.00 UTC (bottom).

which are responsible for the high wind velocities observed (Lancaster et al. 1984). The frequency of these easterly components decreases from inland to the coast. As a result, bidirectional wind regimes within the Namib Sand Sea and at the west Etosha site (Fig. 2a,c,d) and a unidirectional wind regime on the coast at the outlet of the Huab River (Fig. 2b) are observed.

In the case of the Etosha West and Huab stations, the time series of wind speed and direction from the regional predictions quantitatively match those corresponding to the local measurements (Figs. 3, 4 and Online Resource Fig. S5). For the North Sand Sea and South Sand Sea stations within the giant linear dune field, we observe that this agreement is also good, but limited to the October–March time period (Fig. 4a, b, e, f). However, the field-measured wind roses exhibit additional wind components aligned with the dune orientation, as evidenced on the satellite images (Fig. 2c,d).

More precisely, during the April-September period, the local and regional winds in the interdune match during daytime only, i.e when the southerly/southwesterly sea breeze dominates (Figs. 5c,d,g,h and 6). In the late afternoon and during the night, when the easterly ‘berg’ and katabatic winds blow, measurements and predictions differ. In this case, the angular wind distribution of the local measurements exhibits two additional modes corresponding to reversing winds aligned with the dune orientation (purple frame in Fig. 6, Online Resource Fig. S6). This deviation is also associated with a general attenuation of the wind strength (Online Resource Fig. S7). Remarkably, all these figures show that these wind reorientation and attenuation processes occur only at low velocities of the regional wind, typically for $u_*^{\text{ERA5-Land}} \lesssim 0.2 \text{ m s}^{-1}$. For shear velocities larger than $u_*^{\text{ERA5-Land}} \simeq 0.3 \text{ m s}^{-1}$, the wind reorientation is not apparent. Finally, for intermediate shear velocities, both situations of wind flow reoriented along the dune crest and not reoriented can be successively observed (Online Resource Fig. S6). Importantly, these values are not precise thresholds (and certainly not related to the threshold for sediment transport), but indicative of a crossover between regimes, whose physical interpretation is discussed in the next section.

3 Influence of wind speed and circadian cycle on the atmospheric boundary layer

The wind deflection induced by dunes has previously been related to the incident angle between wind direction and crest orientation, with a maximum deflection evident for incident angles between 30° and 70° (Walker et al. 2009; Hesp et al. 2015). In the data analysed here, the most deflected wind at both the North and South Sand Sea stations is seen to be where the incident angle is perpendicular to the giant dunes (Figs. 2 and 6). It therefore appears that in our case, the incident wind angle is not the dominant control on maximum wind deflection. Further, and as shown in Fig. 6, winds of high and low velocities show contrasting behaviour in characteristics of deflection. This suggests a change in hydrodynamical regime between the winds. In this section, we discuss the relevant parameters associated with the dynamical mechanisms that govern the interactions between the atmospheric boundary layer flow and giant dune topographies. This analysis allows us to provide a physics-based interpretation of our measured wind data.

3.1 Flow over a modulated bed

Taking as a reference the turbulent flow over a flat bed, the general framework of our study is understanding and describing the flow response to a bed modulation (e.g. a giant dune). Without loss of generality, we can consider in this context an idealised bed elevation in the form of parallel sinusoidal ridges, with wavelength λ (or wavenumber $k = 2\pi/\lambda$) and amplitude ξ_0 , and where the reference flow direction makes a given incident angle with respect to the ridge

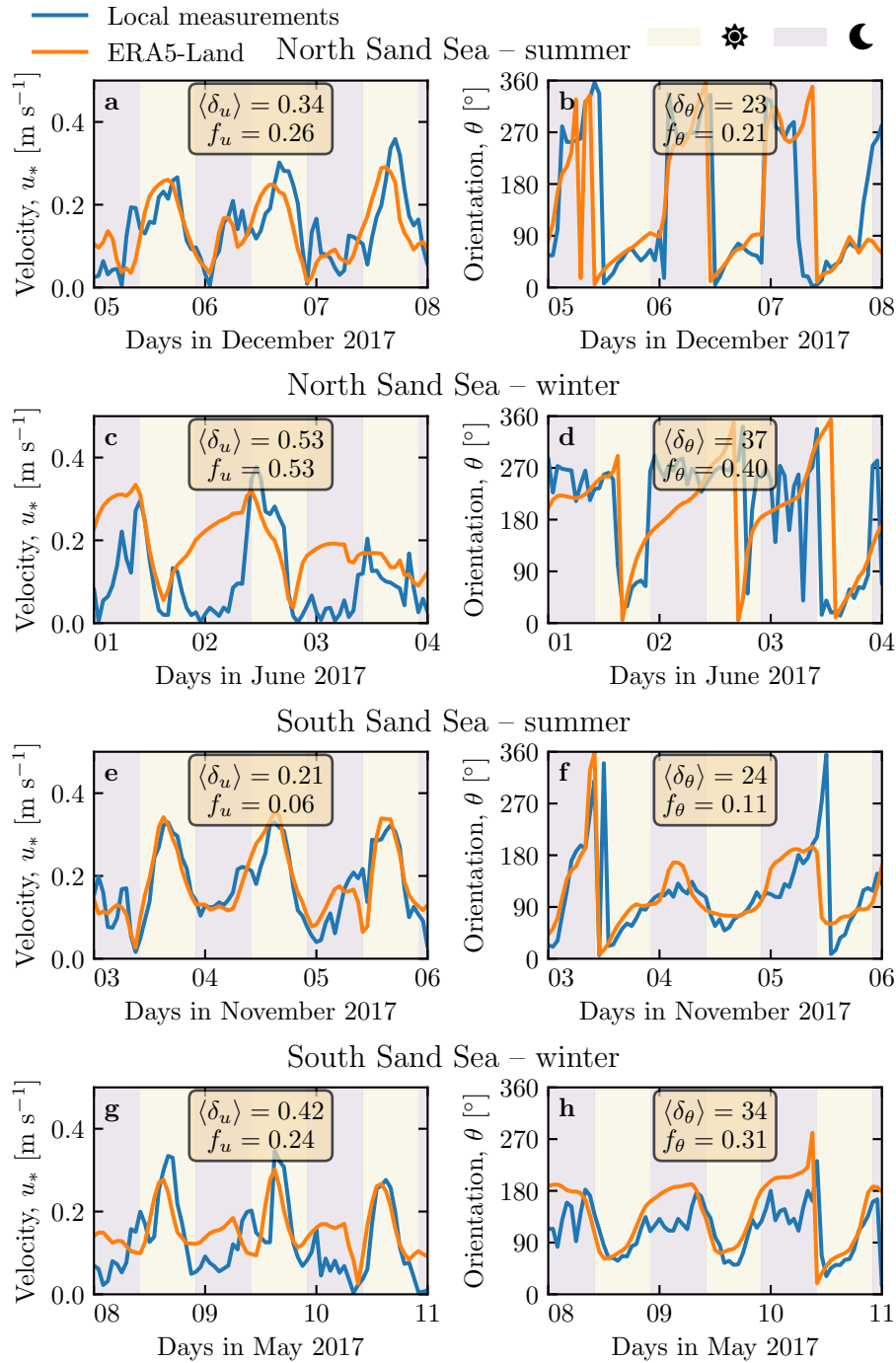


Fig. 5 Same as Fig. 3 for North Sand Sea station in summer (a–b), North Sand Sea station in winter (b–c), South Sand Sea station in summer (d–e) and South Sand Sea station in winter (f–g).

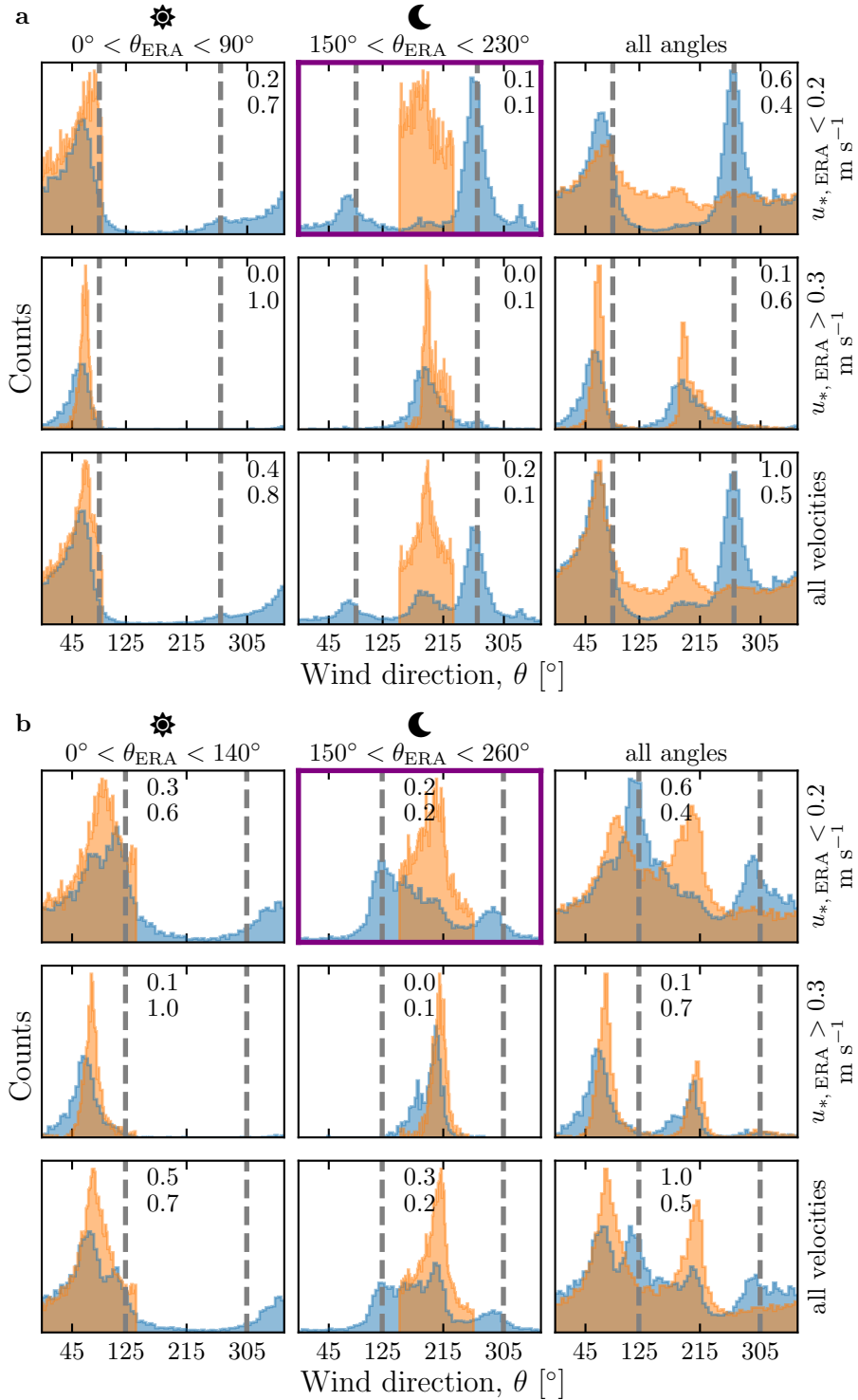


Fig. 6 Same as Fig. 4 but for North Sand Sea (a) and South Sand Sea (b) stations. Here, subplots correspond to different ranges for the wind direction (columns) and wind velocity (rows) of the ERA5-Land dataset. The grey vertical dashed lines indicate the main dune orientation. In contrast with observations at the Huab and Etosha West stations (Fig. 4), histograms do not match well at low wind velocities, and the purple frame highlights the regime (low wind velocities, nocturnal easterly wind) in which the data from both datasets differ most.

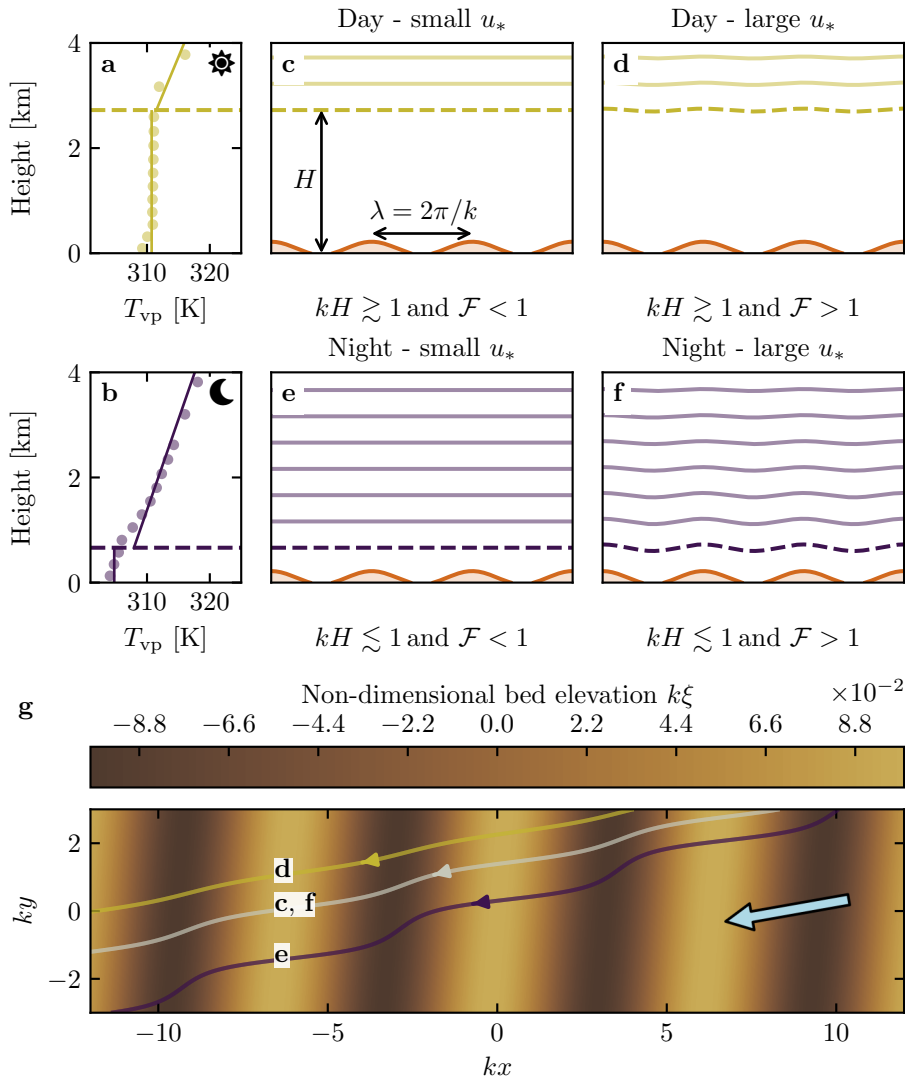


Fig. 7 **a–b:** Vertical profiles of the virtual potential temperature T_{vp} at two different time steps (day - 03/11/2015 - 12.00 UTC, night - 01/13/2013 - 09.00 UTC) at the North Sand Sea station. Dots: data from the ERA5 reanalysis. Dashed lines: boundary layer height given by the ERA5 reanalysis (Online Resource section 2). Plain lines: vertical (boundary layer) and linear (free atmosphere) fits to estimate the stratification properties. **c–f:** Sketches representing the interaction between the giant dunes and the atmospheric flow for different meteorological conditions. **g:** Streamlines over a sinusoidal topography $\xi(x, y)$ qualitatively representing the effect of low, medium and strong flow confinement, in relation to the above panels (see Appendix 4 for more details). The blue arrow indicates the undisturbed wind direction.

crest (Andreotti et al. 2012). Part of this response, on which we focus here, is the flow deflection by the ridges. In a simplified way, it can be understood from the Bernoulli principle (Hesp et al. 2015): as the flow approaches the ridge crest, the compression of the streamlines results in larger flow velocities, and thus lower pressures (Jackson and Hunt 1975). An incident flow oblique to the ridge is then deflected towards lower pressure zones, i.e. towards the crest. Turbulent dissipation tends to increase this effect downstream, resulting in wind deflection along the crest in the lee side (Gadal et al. 2019).

Flow confinement below a capping surface, which enhances streamline compression, has a strong effect on the hydrodynamic response and typically increases flow deflection. This is the case for bedforms forming in open channel flows such as rivers (Kennedy 1963; Chang and Simons 1970; Mizumura 1995; Colombini 2004; Fourrière et al. 2010; Andreotti et al. 2012; Unsworth et al. 2018). This is also relevant for aeolian dunes as they evolve in the turbulent atmospheric boundary layer (ABL) capped by the stratified free atmosphere (FA) (Andreotti et al. 2009). Two main mechanisms, associated with dimensionless numbers must then be considered (Fig. 7). First, topographic obstacles typically disturb the flow over a characteristic height similar to their length. As flow confinement is characterised by a thickness H , the interaction between the dunes and the wind in the ABL is well captured by the parameter kH . The height H is directly related to the sensitive heat flux from the Earth surface. It is typically on the order of a kilometre, but significantly varies with the circadian and seasonal cycles. Emerging and small dunes, with wavelengths in the range 20 to 100 m, are not affected by the flow confinement, corresponding to $kH \gg 1$. For giant dunes with kilometer-scale wavelengths, however, their interaction with the FA can be significant (Andreotti et al. 2009). This translates into a parameter kH in the range 0.02–5, depending on the moment of the day and the season. A second important mechanism is associated with the existence of a thin intermediate so-called capping layer between the ABL and the FA. It is characterised by a density jump $\Delta\rho$, which controls the ‘rigidity’ of this interface, i.e. how much its deformation affects streamline compression. This is usually quantified using the Froude number (Vosper 2004; Stull 2006; Sheridan and Vosper 2006; Hunt et al. 2006; Jiang 2014):

$$\mathcal{F} = \frac{U}{\sqrt{\frac{\Delta\rho}{\rho_0} g H}}, \quad (1)$$

where U is the wind velocity at the top of the ABL and ρ_0 its average density. The intensity of the stratification, i.e. the amplitude of the gradient $|\partial_z \rho|$ in the FA, also impacts the ability to deform the capping layer under the presence of an underlying obstacle, and thus affects the influence of flow confinement. This can be quantified using the internal Froude number (Vosper 2004; Stull 2006; Sheridan and Vosper 2006; Hunt et al. 2006; Jiang 2014) $\mathcal{F}_I = kU/N$, where $N = \sqrt{-g\partial_z \rho / \rho_0}$ is the Brunt-Väisälä frequency (Stull 1988). Both Froude numbers have in practice the same qualitative effect on flow confinement (a

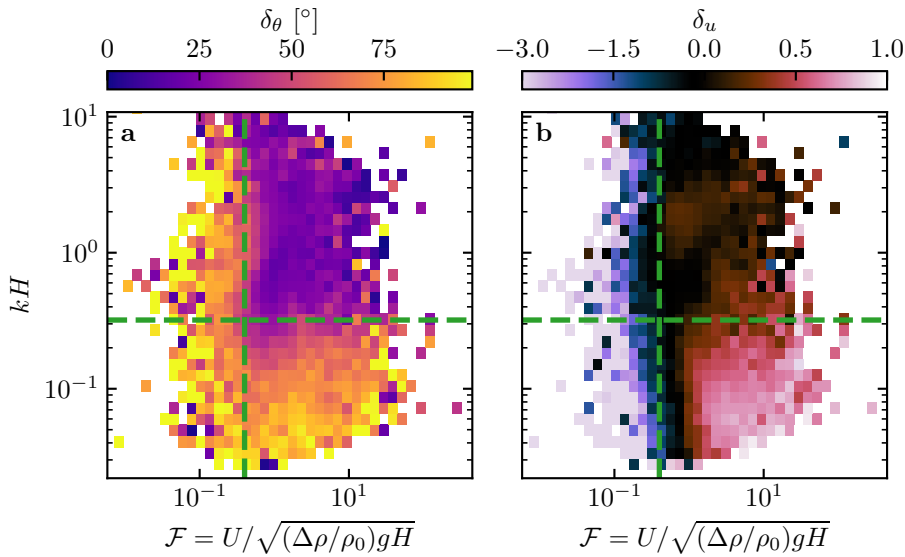


Fig. 8 Regime diagrams of the wind deviation δ_θ (a) and relative attenuation/amplification δ_u (b) in the space (\mathcal{F}, kH) , containing the data from both the North Sand Sea and South Sand Sea stations. The green dashed lines empirically delimit the different regimes. The point density in each bin of the diagrams is shown in Online Resource Fig. S10 – 95% of the data occur in the range $-1 < \delta u < 1$. Similar regime diagrams in the spaces (\mathcal{F}_I, kH) and $(\mathcal{F}_I, \mathcal{F})$ are shown in Online Resource Fig. S11.

277 smaller Froude corresponding to a stiffer interface), and we shall restrict the
278 main discussion to \mathcal{F} only.

279 With this theoretical framework in mind, and in the context of the mea-
280 sured wind data in the North and South Sand Sea stations, the smallest wind
281 disturbances are expected to occur during the day, when the ABL depth is
282 the largest and comparable to the dune wavelength ($kH \gtrsim 1$), which corre-
283 sponds to a weak confinement situation (Fig. 7c,d). In contrast, large wind
284 disturbances are expected to occur during the night, when the confine-
285 ment is mainly induced by a shallow ABL (Fig. 7e). However, this strong confine-
286 ment can be somewhat reduced in the case of strong winds, corresponding to
287 large values of the Froude number and a less ‘rigid’ interface (Fig. 7f). This
288 is in qualitative agreement with the transition from deflected to non-deflected
289 winds related to low and high velocities observed in our data (Sec. 2.2).

290 3.2 Data distribution in the flow regimes

291 We can go one step further and analyse how our data quantitatively spread
292 over the different regimes discussed above. For that purpose, one needs to
293 compute kH and \mathcal{F} from the time series. H , U and the other atmospheric
294 parameters can be deduced from the various vertical profiles (temperature,
295 humidity) available in the ERA5 climate reanalysis (Online Resource section

296 2). We quantify the flow deflection δ_θ as the minimal angle between the wind
 297 orientations comparing the local measurements and the regional predictions.
 298 We also compute the relative velocity modulation as

$$\delta_u = \frac{u_*^{\text{ERA5-Land}} - u_*^{\text{Local mes.}}}{u_*^{\text{ERA5-Land}}}. \quad (2)$$

299 These two quantities are represented as maps in the plane (\mathcal{F}, kH) (Fig. 8a,b),
 300 and one can clearly identify different regions in these plots. Small wind dis-
 301 turbances (small δ_θ and δ_u) are located in the top-right part of the diagrams,
 302 corresponding to a regime with low-interaction as well as low-confinement (kH
 303 and \mathcal{F} large enough, Fig. 7d). Lower values of kH (stronger interaction) or of
 304 Froude number (stronger confinement) both lead to an increase in wind dis-
 305 turbances, both in terms of orientation and velocity. Below a crossover value
 306 $kH \simeq 0.3$, wind disturbance is less sensitive to the \mathcal{F} -value. This is probably
 307 due to enhanced non-linear effects linked to flow modulation by the obstacle
 308 when confinement is strong (e.g. wakes and flow recirculations). The Froude
 309 number also controls a transition from damped to amplified wind velocities
 310 in the interdune, with a crossover around $\mathcal{F} \simeq 0.4$ (Fig. 8b). Such an ampli-
 311 fication is rather unexpected. Checking the occurrence of the corresponding
 312 data, it appears that these amplifications are associated with the southerly
 313 sea breeze, and occur dominantly during the October-March period, when the
 314 other easterly wind is not present (Online Resource Fig. S12a–b). Further-
 315 more, they occur less frequently during the afternoon, and more frequently
 316 at the end of the day (Online Resource Fig. S12c). This effect may be linked
 317 to a change in the flow behaviour in the lee side of the obstacles but further
 318 measurements are needed in order to assess the different possibilities (Baines
 319 1995; Vosper 2004).

320 As the hydrodynamic roughness z_0 determine the magnitude of wind shear
 321 velocities, Froude number \mathcal{F} and relative velocity modulation δ_u , it is impor-
 322 tant to discuss the sensitivity of the results to the z_0 -values chosen for both the
 323 ERA5-Land and the field data (see Online Resource section 4). Other quanti-
 324 ties associated with wind direction are independent of this choice. Considering
 325 the possible range of realistic roughness values, the uncertainty on velocities
 326 estimated using the law of the wall is at most 30 %. A similar maximum un-
 327 certainty applies to the Froude number. This uncertainty also propagates to
 328 δ_u , for which Figure S14 shows that the choice of roughness has little influence
 329 on its temporal variations, even if it can induce a global increase or decrease
 330 of its values. Hence, the choice of the z_0 -values will not qualitatively affect
 331 the overall aspect of the regime diagram presented in Figure 8b. It may only
 332 change the value of δ_u for which the transition between regimes is observed
 333 (dashed green lines in Figure 8b). Our conclusions are thus robust with respect
 334 to the somewhat arbitrary choice of the hydrodynamic roughness values.

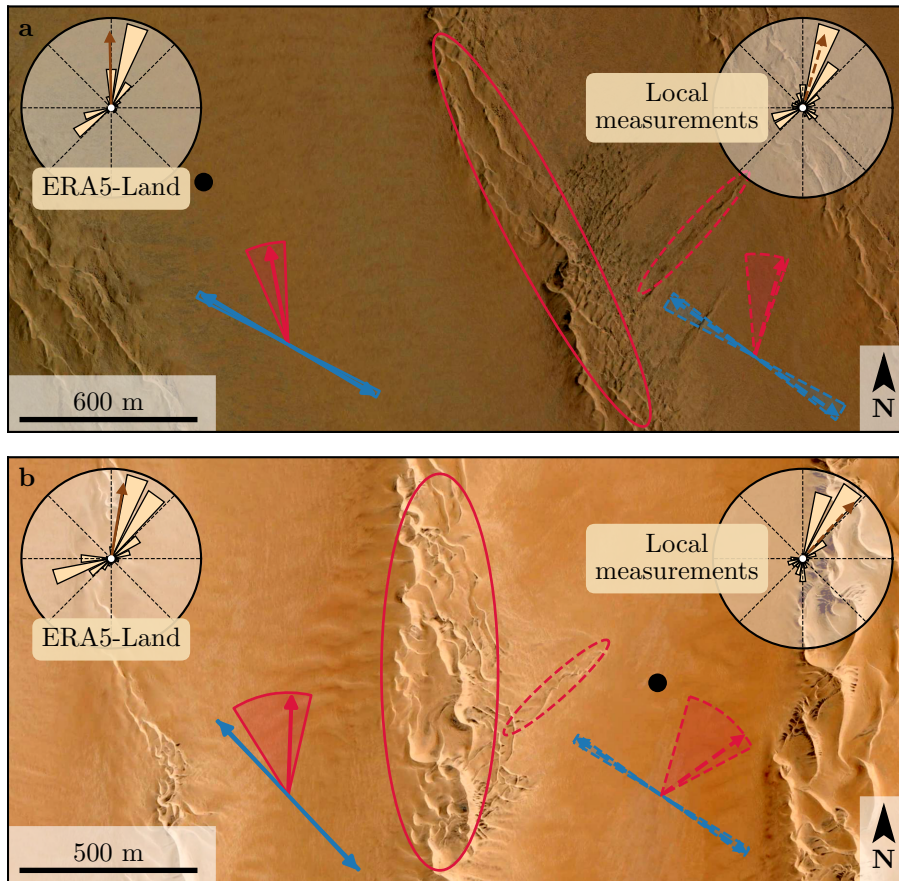


Fig. 9 Implications for smaller scale patterns in (a) the South Sand Sea and (b) North Sand Sea. The ellipses indicate the different types of elongating dunes, at large (plain line) and small (dashed line) scales. Dune orientation are predicted using the model of Courrech du Pont et al. (2014) from the sand flux angular distributions, shown here (roses) along with the resultant transport direction (brown arrow) for typical values (grain size $180 \mu\text{m}$, flux-up ratio of 1.6). Code for corresponding arrows: use of ERA5-Land data (plain line), use of local measurements (dashed line), prediction for the bed instability growth mechanism (blue), prediction for the elongation growth mechanism (red). Wedges show the uncertainty on the orientation calculation when parameters are varied. The black dots indicate the location of the meteorological stations in the interdune. See Appendix 4 for additional details.

335 4 Discussion and conclusion

336 The feedback of the giant dunes on the wind flow has important implications
 337 for smaller scale bedforms. As illustrated in Fig. 9, small linear dunes ($\sim 50 \text{ m}$
 338 wide) are often present within the 1–2 km interdune spaces between giant
 339 linear dunes in the Namib Sand Sea (Livingstone et al. 2010). These smaller
 340 dunes do not exhibit the same orientation as the large ones, and are sometimes
 341 named ‘crossing dunes’ (Chandler et al. 2022). Whilst differences between large

and small scale dune patterns are observed ubiquitously, they are usually attributed to the presence of two different dune growth mechanisms, leading to two different dune patterns (orientations and/or morphologies) for the same wind regime (Courrech du Pont et al. 2014; Runyon et al. 2017; Lü et al. 2017; Song et al. 2019; Gadal et al. 2020; Hu et al. 2021). Here, however, our arguments enable the development of differing orientations for the small and giant linear dunes governed by the same dune growth mechanism (elongating mode). Figure 9 shows how the orientations for the small and giant dunes can be derived from the locally measured and regionally predicted winds respectively (red arrows in Fig. 9). These predictions require the threshold of aeolian sand transport to be specified. Importantly, its value (a shear velocity estimated at $u_{th} \simeq 0.15 \text{ m s}^{-1}$ – see Appendix 4) can be reached in periods during which deflected winds are observed (recall that the stronger winds, responsible for most of the sediment transport and associated dune morphodynamics, are not deflected – see Fig. 6). The feedback of the giant dunes on the wind described in this study, through wind deflection and attenuation, thus provides a potential explanation for the existence of these small linear dunes elongating across the interdune, a dynamic which has remained unresolved to date. These crossing dunes could provide additional constraints for the inference of local winds from bedforms, similarly to that currently performed on Mars using ripple orientations (Liu and Zimbelman 2015; Hood et al. 2021). Further work is needed to investigate these processes in more detail, including measurements of sediment transport and flow on the top of dunes.

This study presents field and reanalysis-based evidence that wind flow patterns around giant dunes are influenced by the atmospheric boundary layer, particularly during nocturnal conditions. However, we do not address here the question of the limitation of the giant dune pattern coarsening, and leave open the debate as to whether their size is controlled by the depth of this layer (Andreotti et al. 2009), in contrast to sediment supply limited and ever-slower growth with size (Werner and Kocurek 1999; Gunn et al. 2022). More field evidence is definitively needed from additional dune fields, but this mechanism would allow for the inference of the ABL depth from giant bedform wavelengths where measurements are not feasible or available, such as Titan (Lorenz et al. 2010).

To conclude on conditions under which the ERA5-Land reanalysis data can reliably be used to study dune morphodynamics, we summarise the comparison of local (direct measurements) and regional (climate reanalysis) wind data as follows. In flat areas, the agreement between the two confirms the ability of the ERA5-Land climate reanalysis to predict the wind regime down to scales $\sim 10 \text{ km}$, i.e the model grid. When smaller scale topographies are present (giant dunes in our case), locally measured winds can significantly differ from the regionally predicted ones. This is the case when the disturbances induced by the dunes interact with the lower part of the ABL vertical structure, which presents circadian variations. During the day, when the capping layer is typically high, this interaction is small, and the ERA5-Land predictions are also quantitatively consistent with the local data. During the night, however, the

388 presence of a shallow atmospheric boundary layer induces a strong confinement
389 of the flow, and is associated with large wind deflection by the dunes.
390 Importantly, we find that this effect can be counterbalanced for large wind
391 velocities, which are capable of deforming the capping layer, thus decreasing
392 the influence of the confinement.

393 The theoretical computation of the wind disturbances induced by sinusoidal ridges under flow confinement has been performed in the linear limit
394 (Andreotti et al. 2009, 2012), i.e. when the aspect ratio of these ridges is small
395 ($k\xi_0 \ll 1$). These models are able to qualitatively reproduce the observed
396 wind deflection (Appendix 4, Online Resource Figs. S11 and S13), and thus
397 provide the physical support for the interpretation we propose here based on
398 hydrodynamic regimes. However, these models cannot quantitatively predict
399 the magnitude of our observations, probably due to the presence of expected
400 non-linearities in high confinement situations linked to strong flow modulations.
401 Besides, these linear calculations only predict wind attenuation in the
402 interdune, in contrast with the observed enhanced velocities associated with
403 particular evening winds from the south during the period October–March
404 (Online Resource Fig. S12). Some other models predict different spatial flow
405 structures in response to a modulated topography, such as lee waves and
406 rotors (Baines 1995; Vosper 2004). However, our measurements are located at a
407 single point in the interdune, and we are thus unable to explore these types of
408 responses. Data at different places along and across the ridges are needed to
409 investigate and possibly map such flow structures, and for further comparisons
410 with the models.

412 **Acknowledgements** We would like to acknowledge the contributors of the following open-
413 source python libraries, Matplotlib (Hunter 2007), Numpy (Harris et al. 2020) and Scipy
414 (Virtanen et al. 2020), which provide an incredibly efficient ecosystem allowing scientific
415 research in Python. We also thank B. Andreotti and A. Gunn for useful discussions.

416 All data used in this study can be found in Gadale et al. (2022). Note that it contains
417 modified Copernicus Climate Change Service Information (2021). Neither the European
418 Commission nor ECMWF is responsible for any use that may be made of the Copernicus
419 Information or Data it contains. Documented codes used in this study to analyse this data are
420 available at <https://github.com/Cgadal/GiantDunes> (will be made public upon acceptance
421 of this manuscript for publication).

422 Multiple grants have supported the collection of wind data through visits to the four
423 sites between 2013 and 2020 (John Fell Oxford University Press (OUP) Research Fund
424 (121/474); National Geographic (CP-029R-17); Natural Environment Research Council UK
425 (NE/R010196/1 and NE/H021841/1 NSFGEO-NERC); Southampton Marine and Maritime
426 Institute SMMI EPSRC-GCRF UK), along with research permits (1978/2014, 2140/2016,
427 2304/2017, 2308/2017, RPIV00022018, RPIV0052018, RPIV00230218). The authors are
428 very grateful for support from Etosha National Park (especially Shyane Kötting, Boas Er-
429 ckie, Pierre du Preez, Claudine Cloete, Immanuel Kapofi, Wilferd Versfeld, and Werner
430 Kilian), Gobabeb Namib Research Institute (Gillian Maggs-Kölling and Eugene Marais),
431 The Skeleton Coast National Park (Joshua Kazeurua). Various researchers and desert en-
432 thusiasts have assisted with instruments and the logistics of expeditions, especially Mary
433 Seely for expert guidance at the North Sand Sea site.

434 Finally, we acknowledge financial support from the Laboratoire d'Excellence UnivEarthS
435 Grant ANR-10-LABX-0023, the Initiative d'Excellence Université de Paris Grant ANR-18-
436 IDEX-0001, the French National Research Agency Grants ANR-17-CE01-0014/SONO and
437 the National Science Center of Poland Grant 2016/23/B/ST10/01700.

438 **Appendix 1: Linear theory of wind response to topographic pertur-**
439 **bation**

440 Following the work of Fourrière et al. (2010), Andreotti et al. (2012) and
441 Andreotti et al. (2009), we briefly describe in this appendix the framework
442 for the linear response of a turbulent flow to a topographic perturbation of
443 small aspect ratio. As a general bed elevation can be decomposed into Fourier
444 modes, we focus here on a sinusoidal topography:

$$\xi = \xi_0 \cos [k (\cos(\alpha)y - \sin(\alpha)x)], \quad (3)$$

445 which is also a good approximation for the giant dunes observed in the North
446 Sand Sea and South Sand Sea Station (Fig. 2 and Online Resource Fig. S4).
447 Here, x and y are the streamwise and spanwise coordinates, $k = 2\pi/\lambda$ the
448 wavenumber of the sinusoidal perturbation, α its crest orientation with respect
449 to the x -direction (anticlockwise) and ξ_0 its amplitude. The two components
450 of the basal shear stress $\tau = \rho_0 u_* \mathbf{u}_*$, constant in the flat bottom reference
451 case, can then be generically written as:

$$\tau_x = \tau_0 \left(1 + k\xi_0 \sqrt{\mathcal{A}_x^2 + \mathcal{B}_x^2} \cos [k (\cos(\alpha)y - \sin(\alpha)x) + \phi_x] \right), \quad (4)$$

$$\tau_y = \tau_0 k\xi_0 \sqrt{\mathcal{A}_y^2 + \mathcal{B}_y^2} \cos [k (\cos(\alpha)y - \sin(\alpha)x) + \phi_y], \quad (5)$$

452 where τ_0 is the reference basal shear stress on a flat bed. We have defined
453 the phase $\phi_{x,y} = \tan^{-1}(\mathcal{B}_{x,y}/\mathcal{A}_{x,y})$ from the in-phase and in-quadrature hy-
454 drodynamical coefficients $\mathcal{A}_{x,y}$ and $\mathcal{B}_{x,y}$. They are functions of k and of the
455 flow conditions, i.e the bottom roughness, the vertical flow structure and the
456 incident flow direction, and the theoretical framework developed in the above
457 cited papers proposes methods to compute them in the linear regime.

458 Following Andreotti et al. (2012), the effect of the incident wind direction
459 can be approximated by the following expressions:

$$\mathcal{A}_x = \mathcal{A}_0 \sin^2 \alpha, \quad (6)$$

$$\mathcal{B}_x = \mathcal{B}_0 \sin^2 \alpha, \quad (7)$$

$$\mathcal{A}_y = -\frac{1}{2} \mathcal{A}_0 \cos \alpha \sin \alpha, \quad (8)$$

$$\mathcal{B}_y = -\frac{1}{2} \mathcal{B}_0 \cos \alpha \sin \alpha, \quad (9)$$

460 where \mathcal{A}_0 and \mathcal{B}_0 are now two coefficients independent of the dune orienta-
461 tion α , corresponding to the transverse case ($\alpha = 90^\circ$). In the case of a fully
462 turbulent boundary layer capped by a stratified atmosphere, these coefficients
463 depend on kH , kz_0 , \mathcal{F} and \mathcal{F}_I (Andreotti et al. 2009). For their computation,
464 we assume here a constant hydrodynamic roughness $z_0 \simeq 1$ mm (Online Re-
465 source section 1). For the considered giant dunes, this leads to $kz_0 \simeq 2 \cdot 10^{-6}$,
466 as their wavelength is $\lambda \simeq 2.4$ km (or $k \simeq 2 \cdot 10^{-3}$ m $^{-1}$). Values of z_0 extracted
467 from field data indeed typically fall between 0.1 mm and 10 mm (Sherman and

468 Farrell 2008; Field and Pelletier 2018). Importantly, \mathcal{A}_0 and \mathcal{B}_0 do not vary
 469 much in the corresponding range of kz_0 (Fourrière et al. 2010), and the results
 470 presented here are robust with respect to this choice.

471 With capping layer height and Froude numbers computed from the ERA5-
 472 Land time series, the corresponding \mathcal{A}_0 and \mathcal{B}_0 can be deduced, as displayed
 473 in Online Resource Fig. S13. Interestingly, it shows similar regimes as in the
 474 diagrams of Fig. 8 and Online Resource Fig. S11a,b, supporting the underlying
 475 physics. However, the agreement is qualitative only. Further, the linearity
 476 assumption of the theoretical framework requires $(|\tau| - \tau_0)/\tau_0 \ll 1$, which
 477 translates into $k\xi\sqrt{\mathcal{A}_0^2 + \mathcal{B}_0^2} \ll 1$. In our case, the giant dune morphology
 478 gives $k\xi_0 \simeq 0.1$, which means that one quits the regime of validity of the
 479 linear theory when the coefficient modulus $\sqrt{\mathcal{A}_0^2 + \mathcal{B}_0^2}$ becomes larger than a
 480 few units. In accordance with the theoretical expectations, these coefficients
 481 present values on the order of unity ($\mathcal{A}_0 \simeq 3$ and $\mathcal{B}_0 \simeq 1$) in unconfined sit-
 482 uations (Claudin et al. 2013; Lü et al. 2021). In contrast and as illustrated
 483 in Online Resource Fig. S13a,b, larger values are predicted in case of strong
 484 confinement, which does not allow us to proceed to further quantitative com-
 485 parison with the data.

486 Finally, the linear model is also able to reproduce the enhancement of the
 487 flow deflection over the sinusoidal ridges when $\sqrt{\mathcal{A}_0^2 + \mathcal{B}_0^2}$ is increased (Online
 488 Resource Fig. S13). Here, using $k\xi_0 \simeq 0.1$ to be representative of the amplitude
 489 of the giant dunes at the North Sand Sea station, the coefficient modulus is
 490 bounded to 10.

491 Appendix 2: Sediment transport and dune morphodynamics

492 We summarise in this appendix the sediment transport and dune morphody-
 493 namics theoretical framework leading to the prediction of sand fluxes and dune
 494 orientations from wind data.

495 *Sediment transport* — The prediction of sand fluxes from wind data has been
 496 a long standing issue in aeolian geomorphological studies (Fryberger and Dean
 497 1979; Pearce and Walker 2005; Sherman and Li 2012; Shen et al. 2019). Based
 498 on laboratory studies in wind tunnels (Rasmussen et al. 1996; Iversen and
 499 Rasmussen 1999; Creysse et al. 2009; Ho et al. 2011), as well as physical
 500 considerations (Ungar and Haff 1987; Andreotti 2004; Durán et al. 2011; Páhtz
 501 and Durán 2020), it has been shown that the steady saturated saltation flux
 502 over a flat sand bed depends linearly on the shear stress:

$$\frac{q_{\text{sat}}}{Q} = \Omega \sqrt{\Theta_{\text{th}}} (\Theta - \Theta_{\text{th}}), \quad (10)$$

503 where Ω is a proportionality constant, $Q = d\sqrt{(\rho_s - \rho_0)gd/\rho_0}$ is a character-
 504 istic flux, $\Theta = \rho_0 u_*^2 / (\rho_s - \rho_0)gd$ the Shields number, and Θ_{th} its threshold
 505 value below which saltation vanishes. $\rho_s = 2.6 \text{ g cm}^{-3}$ and $d = 180 \mu\text{m}$ are
 506 the grain density and diameter, and g is the gravitational acceleration. The

shear velocity, and consequently the Shields number as well as the sediment flux, are time dependent.

Recently, Pähzt and Durán (2020) suggested an additional quadratic term in Shields to account for grain-grain interactions within the transport layer at strong wind velocities:

$$\frac{q_{\text{sat}, t}}{Q} = \frac{2\sqrt{\Theta_{\text{th}}}}{\kappa\mu} (\Theta - \Theta_{\text{th}}) \left(1 + \frac{C_M}{\mu} [\Theta - \Theta_{\text{th}}] \right), \quad (11)$$

where $\kappa = 0.4$ is the von Kármán constant, $C_M \simeq 1.7$ a constant and $\mu \simeq 0.6$ is a friction coefficient, taken to be the avalanche slope of the granular material. The fit of this law to the experimental data of Creyssels et al. (2009) and Ho et al. (2011) gives $\Theta_{\text{th}} = 0.0035$. The fit of Eq. 10 on these same data similarly gives $\Omega \simeq 8$ and $\Theta_{\text{th}} = 0.005$. The sand flux angular distributions and the dune orientations in Fig. 9 are calculated using this law (11). We have checked that using the ordinary linear relationship (10) instead does not change the predicted dune orientations by more than a few degrees.

Dune orientations — Dune orientations are predicted with the dimensional model of Courrech du Pont et al. (2014), from the sand flux time series computed with the above transport law. Two orientations are possible depending on the mechanism dominating the dune growth: elongation or bed instability. The orientation α corresponding to the bed instability is then the one that maximises the following growth rate (Rubin and Hunter 1987):

$$\sigma \propto \frac{1}{H_d W_d T} \int_0^T q_{\text{crest}} |\sin(\theta - \alpha)| dt, \quad (12)$$

where θ is the wind orientation measured with respect to the same reference as α , and H_d and W_d are dimensional constants respectively representing the dune height and width. The integral runs over a time T , which must be representative of the characteristic period of the wind regime. The flux at the crest is expressed as:

$$q_{\text{crest}} = q_{\text{sat}} [1 + \gamma |\sin(\theta - \alpha)|], \quad (13)$$

where the flux-up ratio γ has been calibrated to 1.6 using field studies, underwater laboratory experiments and numerical simulations. Predictions of the linear analysis of Gadal et al. (2019) and Delorme et al. (2020) give similar results.

Similarly, the dune orientation corresponding to the elongation mechanism is the one that verifies:

$$\tan(\alpha) = \frac{\langle q_{\text{crest}}(\alpha) \mathbf{e}_\theta \rangle \cdot \mathbf{e}_{WE}}{\langle q_{\text{crest}}(\alpha) \mathbf{e}_\theta \rangle \cdot \mathbf{e}_{SN}}, \quad (14)$$

where $\langle \cdot \rangle$ denotes a vectorial time average. The unitary vectors \mathbf{e}_{WE} , \mathbf{e}_{SN} and \mathbf{e}_θ are in the West-East, South-North and wind directions, respectively.

The resulting computed dune orientations, blue and red arrows in Fig. 9, then depend on a certain number of parameters (grain properties, flux-up ratio,

etc.), for which we take typical values for aeolian sandy deserts. Due to the lack of measurements in the studied places, some uncertainties can be expected. We therefore run a sensitivity test by calculating the dune orientations for grain diameters ranging from $100 \mu\text{m}$ to $400 \mu\text{m}$ and for a speed-up ratio between 0.1 and 10 (wedges in Fig. 9).

References

- 547 Andreotti B (2004) A two-species model of aeolian sand transport. *J Fluid
548 Mech* 510:47–70
- 549 Andreotti B, Claudin P, Douady S (2002) Selection of dune shapes and veloc-
550 ities part 1: Dynamics of sand, wind and barchans. *The European Physical
551 Journal B-Condensed Matter and Complex Systems* 28:321–339
- 552 Andreotti B, Fourrière A, Ould-Kaddour F, Murray B, Claudin P (2009) Gi-
553 ant aeolian dune size determined by the average depth of the atmospheric
554 boundary layer. *Nature* 457:1120–1123
- 555 Andreotti B, Claudin P, Devauchelle O, Durán O, Fourrière A (2012) Bedforms
556 in a turbulent stream: ripples, chevrons and antidunes. *J Fluid Mech* 690:94–
557 128
- 558 Ashkenazy Y, Yizhaq H, Tsoar H (2012) Sand dune mobility under climate
559 change in the kalahari and australian deserts. *Climatic Change* 112:901–923
- 560 Baddock M, Livingstone I, Wiggs G (2007) The geomorphological significance
561 of airflow patterns in transverse dune interdunes. *Geomorphology* 87:322–
562 336
- 563 Bagnold RA (1941) *The Physics of Blown Sand and Desert Dunes*. London :
564 Methuen : Chapman & Hall
- 565 Baines PG (1995) Topographic effects in stratified flows. Cambridge university
566 press
- 567 Bauer BO, Sherman DJ, Wolcott JF (1992) Sources of uncertainty in shear
568 stress and roughness length estimates derived from velocity profiles. *The
569 Professional Geographer* 44:453–464
- 570 Belcher S, Hunt J (1998) Turbulent flow over hills and waves. *Annu Rev Fluid
571 Mech* 30:507–538
- 572 Blumberg DG, Greeley R (1996) A comparison of general circulation model
573 predictions to sand drift and dune orientations. *J Clim* 9:3248–3259
- 574 Bristow NR, Best J, Wiggs GFS, Nield JM, Baddock MC, Delorme P, Chris-
575 tensen KT (2022) Topographic perturbation of turbulent boundary layers
576 by low-angle, early-stage aeolian dunes. *Earth Surf Process Landf* n/a, DOI
577 <https://doi.org/10.1002/esp.5326>
- 578 Brookfield M (1977) The origin of bounding surfaces in ancient aeolian sand-
579 stones. *Sedimentology* 24:303–332
- 580 Brown S, Nickling WG, Gillies JA (2008) A wind tunnel examination of shear
581 stress partitioning for an assortment of surface roughness distributions. *J
582 Geophys Res* 113:F02S06
- 583 Chandler C, Radebaugh J, McBride J, Morris T, Narteau C, Arnold K, Lorenz
584 R, Barnes J, Hayes A, Rodriguez S, Rittenour T (2022) Near-surface struc-
585 ture of a large linear dune and an associated crossing dune of the northern
586 Namib Sand Sea from ground penetrating radar: Implications for the his-
587 tory of large linear dunes on Earth and Titan. *Aeolian Research* 57:100813,
588 DOI <https://doi.org/10.1016/j.aeolia.2022.100813>
- 589 Chang H, Simons D (1970) The bed configuration of straight sand-bed channels
590 when flow is nearly critical. *J Fluid Mech* 42:491–495

- 591 Charru F, Andreotti B, Claudin P (2013) Sand ripples and dunes. *Annu Rev Fluid Mech* 45:469–493
- 593 Claudin P, Wiggs G, Andreotti B (2013) Field evidence for the upwind velocity shift at the crest of low dunes. *Boundary-Layer Meteorol* 148:195–206
- 595 Claudin P, Durán O, Andreotti B (2017) Dissolution instability and roughening transition. *J Fluid Mech* 832:R2
- 597 Claudin P, Louge M, Andreotti B (2021) Basal pressure variations induced by a turbulent flow over a wavy surface. *Frontiers in Physics* 9:682564
- 599 Colombini M (2004) Revisiting the linear theory of sand dune formation. *J Fluid Mech* 502:1–16
- 601 Courrech du Pont S (2015) Dune morphodynamics. *C R Phys* 16:118–138
- 602 Courrech du Pont S, Narteau C, Gao X (2014) Two modes for dune orientation. *Geology* 42:743–746
- 604 Creyssels M, Dupont P, El Mohtar AO, Valance A, Cantat I, Jenkins JT, Pasini JM, Rasmussen KR (2009) Saltating particles in a turbulent boundary layer: experiment and theory. *J Fluid Mech* 625:47–74
- 607 de Winter W, Donker J, Sterk G, Van Beem J, Ruessink G (2020) Regional versus local wind speed and direction at a narrow beach with a high and steep foredune. *Plos one* 15:e0226983
- 610 Dee DP, Uppala SM, Simmons AJ, Berrisford P, Poli P, Kobayashi S, Andrae U, Balmaseda M, Balsamo G, Bauer dP, et al. (2011) The ERA-Interim reanalysis: Configuration and performance of the data assimilation system. *Q J R Meteorol Soc* 137:553–597
- 614 Delorme P, Wiggs G, Baddock M, Claudin P, Nield J, Valdez A (2020) Dune initiation in a bimodal wind regime. *J Geophys Res* 125:e2020JF005757
- 616 Durán O, Claudin P, Andreotti B (2011) On aeolian transport: Grain-scale interactions, dynamical mechanisms and scaling laws. *Aeolian Res* 3:243–270
- 619 Durran DR (1990) Mountain waves and downslope winds. In: *Atmospheric processes over complex terrain*, Springer, pp 59–81
- 621 Dyer A (1974) A review of flux-profile relationships. *Boundary-Layer Meteorol* 7:363–372
- 623 Ewing RC, Kocurek G, Lake LW (2006) Pattern analysis of dune-field parameters. *Earth Surf Process Landf* 31:1176–1191
- 625 Farr TG, Rosen PA, Caro E, Crippen R, Duren R, Hensley S, Kobrick M, Paller M, Rodriguez E, Roth L, et al. (2007) The shuttle radar topography mission. *Rev Geophys* 45
- 628 Fernando H, Mann J, Palma J, Lundquist JK, Barthelmie RJ, Belo-Pereira M, Brown W, Chow F, Gerz T, Hocut C, et al. (2019) The perdigão: Peering into microscale details of mountain winds. *Bull Am Meteorol Soc* 100:799–819
- 632 Field JP, Pelletier JD (2018) Controls on the aerodynamic roughness length and the grain-size dependence of aeolian sediment transport. *Earth Surf Process Landf* 43:2616–2626
- 635 Finnigan J, Raupach M, Bradley E, Aldis G (1990) A wind tunnel study of turbulent flow over a two-dimensional ridge. *Boundary-Layer Meteorol*

- 637 50:277–317
- 638 Finnigan J, Ayotte K, Harman I, Katul G, Oldroyd H, Patton E, Poggi D,
639 Ross A, Taylor P (2020) Boundary-layer flow over complex topography.
640 *Boundary-Layer Meteorol* 177:247–313
- 641 Flack K, Schultz M (2010) Review of hydraulic roughness scales in the fully
642 rough regime. *Journal of Fluids Engineering* 132:041203
- 643 Fourrière A, Claudin P, Andreotti B (2010) Bedforms in a turbulent stream:
644 formation of ripples by primary linear instability and of dunes by nonlinear
645 pattern coarsening. *J Fluid Mech* 649:287–328
- 646 Frederick KA, Hanratty TJ (1988) Velocity measurements for a turbulent non-
647 separated flow over solid waves. *Exp Fluids* 6:477–486
- 648 Fryberger SG, Dean G (1979) Dune forms and wind regime. A study of global
649 sand seas 1052:137–169
- 650 Gadal C, Narteau C, Courrech Du Pont S, Rozier O, Claudin P (2019) Incip-
651 ient bedforms in a bidirectional wind regime. *J Fluid Mech* 862:490–516
- 652 Gadal C, Narteau C, Courrech du Pont S, Rozier O, Claudin P (2020) Peri-
653 odicity in fields of elongating dunes. *Geology* 48:343–347
- 654 Gadal C, Delorme P, Narteau C, Wiggs G, Baddock M, Nield JM, Claudin
655 P (2022) Data used in 'Local wind regime induced by giant linear dunes:
656 comparison of ERA5-Land re-analysis with surface measurements'. DOI
657 10.5281/zenodo.6343138
- 658 Gao X, Narteau C, Gadal C (2021) Migration of reversing dunes against the
659 sand flow path as a singular expression of the speed-up effect. *Journal of
660 Geophysical Research: Earth Surface* 126(5):e2020JF005913
- 661 Garratt JR (1994) The atmospheric boundary layer. *Earth-Science Reviews*
662 37:89–134
- 663 Garvey B, Castro IP, Wiggs G, Bullard J (2005) Measurements of flows over
664 isolated valleys. *Boundary-Layer Meteorol* 117:417–446
- 665 Gong W, Ibbetson A (1989) A wind tunnel study of turbulent flow over model
666 hills. *Boundary-Layer Meteorol* 49:113–148
- 667 Gong W, Taylor P, Dörnbrack A (1996) Turbulent boundary-layer flow over
668 fixed aerodynamically rough two-dimensional sinusoidal waves. *J Fluid Mech*
669 312:1–37
- 670 Guérin A, Derr J, Du Pont SC, Berhanu M (2020) Streamwise dissolution
671 patterns created by a flowing water film. *Phys Rev Lett* 125:194502
- 672 Gunn A, Wanker M, Lancaster N, Edmonds D, Ewing R, Jerolmack
673 D (2021) Circadian rhythm of dune-field activity. *Geophys Res Lett*
674 48:e2020GL090924
- 675 Gunn A, Casasanta G, Di Liberto L, Falcini F, Lancaster N, Jerolmack DJ
676 (2022) What sets aeolian dune height? *Nature communications* 13(1):1–8
- 677 Harris CR, Millman KJ, van der Walt SJ, Gommers R, Virtanen P, Cournapeau
678 D, Wieser E, Taylor J, Berg S, Smith NJ, et al. (2020) Array program-
679 ming with numpy. *Nature* 585:357–362
- 680 Havholm KG, Kocurek G (1988) A preliminary study of the dynamics of
681 a modern draa, Algodones, southeastern California, USA. *Sedimentology*
682 35:649–669

- 683 Hersbach H, Bell B, Berrisford P, Hirahara S, Horányi A, Muñoz-Sabater J,
684 Nicolas J, Peubey C, Radu R, Schepers D, et al. (2020) The ERA5 global
685 reanalysis. *Q J R Meteorol Soc* 146:1999–2049
- 686 Hesp P, Illenberger W, Rust I, McLachlan A, Hyde R (1989) Some aspects of
687 transgressive dunefield and transverse dune geomorphology and dynamics,
688 south coast, South Africa. *Zeitschrift fur Geomorphologie*, Supplementband
689 73:111–123
- 690 Hesp PA, Hastings K (1998) Width, height and slope relationships and aero-
691 dynamic maintenance of barchans. *Geomorphology* 22:193–204
- 692 Hesp PA, Smyth TAG, Nielsen P, Walker IJ, Bauer BO, Davidson-Arnott R
693 (2015) Flow deflection over a foredune. *Geomorphology* 230:64–74
- 694 Ho TD, Valance A, Dupont P, Ould El Moctar A (2011) Scaling laws in aeolian
695 sand transport. *Phys Rev Lett* 106:4–7
- 696 Hood DR, Ewing RC, Roback KP, Runyon K, Avouac JP, McEnroe M (2021)
697 Inferring airflow across martian dunes from ripple patterns and dynamics.
698 *Frontiers in Earth Science* 9:702828
- 699 Howard AD (1977) Effect of slope on the threshold of motion and its applica-
700 tion to orientation of wind ripples. *Geological Society of America Bulletin*
701 88:853–856
- 702 Hu Z, Gao X, Lei J, Zhou N (2021) Geomorphology of aeolian dunes in the
703 western Sahara Desert. *Geomorphology* 392:107916
- 704 Hunt J, Leibovich S, Richards K (1988) Turbulent shear flows over low hills.
705 *Q J R Meteorol Soc* 114:1435–1470
- 706 Hunt JCR, Vilenski GG, Johnson ER (2006) Stratified separated flow around
707 a mountain with an inversion layer below the mountain top. *J Fluid Mech*
708 556:105–119
- 709 Hunter JD (2007) Matplotlib: A 2d graphics environment. *Computing in sci-
710 ence & engineering* 9:90–95
- 711 Hunter RE, Richmond BM, Alpha TR (1983) Storm-controlled oblique dunes
712 of the Oregon coast. *Geol Soc America Bull* 94:1450–1465
- 713 Iversen JD, Rasmussen KR (1999) The effect of wind speed and bed slope on
714 sand transport. *Sedimentology* 46:723–731
- 715 Jackson PS, Hunt JCR (1975) Turbulent wind flow over a low hill. *Q J R
716 Meteorol Soc* 101:929–955
- 717 Jiang Q (2014) Applicability of reduced-gravity shallow-water theory to atmo-
718 spheric flow over topography. *J Atmos Sci* 71:1460–1479
- 719 Jolivet M, Braucher R, Dovchintseren D, Hocquet S, Schmitt J, ASTER Team
720 (2021) Erosion around a large-scale topographic high in a semi-arid sedimen-
721 tary basin: Interactions between fluvial erosion, aeolian erosion and aeolian
722 transport. *Geomorphology* 386:107747
- 723 Kennedy JF (1963) The mechanics of dunes and antidunes in erodible-bed
724 channels. *J Fluid Mech* 16:521–544
- 725 Kim HG, Patel VC, Lee CM (2000) Numerical simulation of wind flow over
726 hilly terrain. *J Wind Eng Ind Aerodyn* 87:45–60
- 727 Kroy K, Sauermann G, Herrmann HJ (2002) Minimal model for aeolian sand
728 dunes. *Phys Rev E* 66:031302

- 729 Lancaster J, Lancaster N, Seely M (1984) Climate of the central Namib desert.
730 Madoqua 1984:5–61
- 731 Lancaster N (1985) Winds and sand movements in the Namib sand sea. *Earth
732 Surf Process Landf* 10:607–619
- 733 Lancaster N, Nickling W, Neuman CM, Wyatt V (1996) Sediment flux and
734 airflow on the stoss slope of a barchan dune. *Geomorphology* 17:55–62
- 735 Lewis HW, Mobbs SD, Lehning M (2008) Observations of cross-ridge flows
736 across steep terrain. *Q J R Meteorol Soc* 134:801–816
- 737 Liu ZYC, Zimbelman JR (2015) Recent near-surface wind directions inferred
738 from mapping sand ripples on martian dunes. *Icarus* 261:169–181
- 739 Livingstone I, Warren A (2019) Aeolian geomorphology: a new introduction.
740 Wiley
- 741 Livingstone I, Bristow C, Bryant RG, Bullard J, White K, Wiggs GFS, Baas
742 ACW, Bateman MD, Thomas DSG (2010) The Namib Sand Sea digital
743 database of aeolian dunes and key forcing variables. *Aeolian Res* 2:93–104
- 744 Lorenz R, Claudin P, Andreotti B, Radebaugh J, Tokano T (2010) A 3 km at-
745 mospheric boundary layer on Titan indicated by dune spacing and Huygens
746 data. *Icarus* 205:719–721
- 747 Lü P, Narteau C, Dong Z, Rozier O, Du Pont SC (2017) Unravelling raked
748 linear dunes to explain the coexistence of bedforms in complex dunefields.
749 *Nature Communications* 8:1–9
- 750 Lü P, Narteau C, Dong Z, Claudin P, Rodriguez S, An Z, Fernandez-Cascales
751 L, Gadal C, Courrech du Pont S (2021) Direct validation of dune instability
752 theory. *Proceedings of the National Academy of Sciences* 118
- 753 Mason P, Sykes R (1979) Flow over an isolated hill of moderate slope. *Q J R
754 Meteorol Soc* 105:383–395
- 755 McKenna Neuman C, Lancaster N, Nickling WG (1997) Relations between
756 dune morphology, air flow, and sediment flux on reversing dunes, Silver Peak,
757 Nevada. *Sedimentology* 44:1103–1111, DOI 10.1046/j.1365-3091.1997.d01-
758 61.x
- 759 Mizumura K (1995) Free-surface profile of open-channel flow with wavy bound-
760 ary. *J Hydraul Eng* 121:533–539
- 761 Monin AS, Obukhov AM (1954) Basic laws of turbulent mixing in the surface
762 layer of the atmosphere. *Contrib Geophys Inst Acad Sci USSR* 151:e187
- 763 Mulligan KR (1988) Velocity profiles measured on the windward slope of a
764 transverse dune. *Earth Surf Process Landf* 13:573–582
- 765 Muñoz-Sabater J, Dutra E, Agustí-Panareda A, Albergel C, Arduini G, Bal-
766 samo G, Boussetta S, Choulga M, Harrigan S, Hersbach H, et al. (2021)
767 ERA5-Land: A state-of-the-art global reanalysis dataset for land applica-
768 tions. *Earth Syst Sci Data* 13:4349–4383
- 769 Nield JM, King J, Wiggs GFS, Leyland J, Bryant RG, Chiverrell RC, Darby
770 SE, Eckhardt FD, Thomas DSG, Vircavs LH, Washington R (2014) Esti-
771 mating aerodynamic roughness over complex surface terrain. *J Geophys Res*
772 118:12948–12961
- 773 Nield JM, Wiggs GG, Baddock MC, Hipondoka MH (2017) Coupling lee-
774 side rainfall to avalanche characteristics in aeolian dune dynamics. *Geology*

- 775 45:271–274
- 776 Pähzt T, Durán O (2020) Unification of aeolian and fluvial sediment transport
777 rate from granular physics. *Phys Rev Lett* 124:168001
- 778 Pearce KI, Walker IJ (2005) Frequency and magnitude biases in the 'Fryberger'
779 model, with implications for characterizing geomorphically effective winds.
780 *Geomorphology* 68:39–55
- 781 Pelletier JD, Field JP (2016) Predicting the roughness length of turbulent flows
782 over landscapes with multi-scale microtopography. *Earth Surface Dynamics*
783 4:391–405
- 784 Poggi D, Katul G, Albertson J, Ridolfi L (2007) An experimental investigation
785 of turbulent flows over a hilly surface. *Phys Fluids* 19:036601
- 786 Rasmussen KR (1989) Some aspects of flow over coastal dunes. *Proceedings of*
787 *the Royal Society of Edinburgh, Section B: Biological Sciences* 96:129–147
- 788 Rasmussen KR, Iversen JD, Rautaheimo P (1996) Saltation and wind flow
789 interaction in a variable slope wind tunnel. *Geomorphology* 17:19–28
- 790 Raupach M (1992) Drag and drag partition on rough surfaces. *Boundary-Layer*
791 *Meteorol* 60:375–395
- 792 Rozier O, Narteau C, Gadal C, Claudin P, Courrech du Pont S (2019)
793 Elongation and stability of a linear dune. *Geophysical Research Letters*
794 46(24):14521–14530
- 795 Rubin DM, Hunter RE (1987) Bedform alignment in directionally varying
796 flows. *Science* 237:276–278
- 797 Runyon K, Bridges N, Ayoub F, Newman C, Quade J (2017) An integrated
798 model for dune morphology and sand fluxes on Mars. *Earth and Planetary*
799 *Science Letters* 457:204–212
- 800 Sauermann G, Andrade Jr J, Maia L, Costa U, Araújo A, Herrmann H
801 (2003) Wind velocity and sand transport on a barchan dune. *Geomorphology*
802 54:245–255
- 803 Seidel DJ, Zhang Y, Beljaars A, Golaz JC, Jacobson AR, Medeiros B (2012)
804 Climatology of the planetary boundary layer over the continental United
805 States and Europe. *J Geophys Res* 117:D17106
- 806 Shao Y (2008) Physics and modelling of wind erosion, vol 37. Springer Science
807 & Business Media
- 808 Shen Y, Zhang C, Huang X, Wang X, Cen S (2019) The effect of wind speed
809 averaging time on sand transport estimates. *Catena* 175:286–293
- 810 Sheridan PF, Vosper SB (2006) A flow regime diagram for forecasting lee
811 waves, rotors and downslope winds. *Meteorol Appl* 13:179–195
- 812 Sherman CA (1978) A mass-consistent model for wind fields over complex
813 terrain. *J Appl Meteorol Clim* 17:312–319
- 814 Sherman D, Farrell E (2008) Aerodynamic roughness lengths over movable
815 beds: Comparison of wind tunnel and field data. *J Geophys Res* 113:1–10
- 816 Sherman DJ, Li B (2012) Predicting aeolian sand transport rates: A reevalu-
817 ation of models. *Aeolian Res* 3:371–378
- 818 Smith AB, Jackson DWT, Cooper JAG (2017) Three-dimensional airflow and
819 sediment transport patterns over barchan dunes. *Geomorphology* 278:28–42

- 820 Song Q, Gao X, Lei J, Li S (2019) Spatial distribution of sand dunes and their
821 relationship with fluvial systems on the southern margin of the Taklimakan
822 Desert, China. *Geomatics, Natural Hazards and Risk* 10:2408–2428
- 823 Spalding DB (1961) A single formula for the law of the wall. *Journal of Applied
824 Mechanics* 28:455–458
- 825 Stull R (2006) 9 - the atmospheric boundary layer. In: Wallace JM, Hobbs PV
826 (eds) *Atmospheric Science* (Second Edition), second edition edn, Academic
827 Press, San Diego, pp 375–417
- 828 Stull RB (1988) An introduction to boundary layer meteorology, vol 13.
829 Springer Science & Business Media
- 830 Sullivan PP, McWilliams JC (2010) Dynamics of winds and currents coupled
831 to surface waves. *Annu Rev Fluid Mech* 42:19–42
- 832 Sweet M, Kocurek G (1990) An empirical model of aeolian dune lee-face air-
833 flow. *Sedimentology* 37:1023–1038
- 834 Sykes RI (1980) An asymptotic theory of incompressible turbulent boundary-
835 layer flow over a small hump. *J Fluid Mech* 101:647–670
- 836 Taylor P, Teunissen H (1987) The Askervein hill project: overview and back-
837 ground data. *Boundary-Layer Meteorol* 39:15–39
- 838 Taylor P, Mason P, Bradley E (1987) Boundary-layer flow over low hills.
839 *Boundary-Layer Meteorol* 39:107–132
- 840 Tsoar H, Yaalon DH (1983) Deflection of sand movement on a sinuous longi-
841 tudinal (seif) dune: use of fluorescent dye as tracer. *Sedimentary Geology*
842 36:25–39
- 843 Ungar JE, Haff PK (1987) Steady state saltation in air. *Sedimentology* 34:289–
844 299
- 845 Unsworth C, Parsons D, Hardy R, Reesink A, Best J, Ashworth P, Keevil G
846 (2018) The impact of nonequilibrium flow on the structure of turbulence
847 over river dunes. *Water Resour Res* 54:6566–6584
- 848 Uppala SM, Källberg P, Simmons AJ, Andrae U, Bechtold VDC, Fiorino M,
849 Gibson J, Haseler J, Hernandez A, Kelly G, et al. (2005) The ERA-40 re-
850 analysis. *Q J R Meteorol Soc* 131:2961–3012
- 851 Valance A, Rasmussen K, Ould El Moctar A, Dupont P (2015) The physics
852 of aeolian sand transport. *C R Phys* 16:1–13
- 853 Venditti JG, Best JL, Church M, Hardy RJ (2013) Coherent Flow Structures
854 at Earth's Surface. John Wiley & Sons
- 855 Virtanen P, Gommers R, Oliphant TE, Haberland M, Reddy T, Cournapeau
856 D, Burovski E, Peterson P, Weckesser W, Bright J, et al. (2020) Scipy 1.0:
857 fundamental algorithms for scientific computing in python. *Nature methods*
858 17:261–272
- 859 Vogelezang D, Holtslag A (1996) Evaluation and model impacts of alternative
860 boundary-layer height formulations. *Boundary-Layer Meteorol* 81:245–269
- 861 Vosper SB (2004) Inversion effects on mountain lee waves. *Q J R Meteorol Soc*
862 130:1723–1748
- 863 Walker I, Davidson-Arnott R, Bauer B, Hesp P, Delgado-Fernandez I, Oller-
864 head J, Smyth T (2017) Scale-dependent perspectives on the geomorphology
865 and evolution of beach-dune systems. *Earth-Science Review* 171:220–253

- 866 Walker IJ, Nickling WG (2002) Dynamics of secondary airflow and sediment
867 transport over and in the lee of transverse dunes. *Prog Phys Geogr* 26:47–75
- 868 Walker IJ, Hesp PA, Davidson-Arnott RG, Ollerhead J (2006) Topographic
869 steering of alongshore airflow over a vegetated foredune: Greenwich Dunes,
870 Prince Edward Island, Canada. *Journal of Coastal Research* 22:1278–1291
- 871 Walker IJ, Hesp PA, Davidson-Arnott RG, Bauer BO, Namikas SL, Ollerhead
872 J (2009) Responses of three-dimensional flow to variations in the angle of
873 incident wind and profile form of dunes: Greenwich Dunes, Prince Edward
874 Island, Canada. *Geomorphology* 105:127–138
- 875 Walmsley JL, Salmon J, Taylor P (1982) On the application of a model of
876 boundary-layer flow over low hills to real terrain. *Boundary-Layer Meteorol*
877 23:17–46
- 878 Weaver C, Wiggs G (2011) Field measurements of mean and turbulent airflow
879 over a barchan sand dune. *Geomorphology* 128:32–41
- 880 Werner BT, Kocurek G (1999) Bedform spacing from defect dynamics. *Geol-*
881 *ogy* 27:727–730
- 882 Wiggs G, Bullard J, Garvey B, Castro I (2002) Interactions between airflow
883 and valley topography with implications for aeolian sediment transport.
884 *Physical Geography* 23:366–380
- 885 Wood N (2000) Wind flow over complex terrain: a historical perspective and
886 the prospect for large-eddy modelling. *Boundary-Layer Meteorol* 96:11–32
- 887 Zhang C, Li Q, Zhou N, Zhang J, Kang L, Shen Y, Jia W (2016) Field obser-
888 vations of wind profiles and sand fluxes above the windward slope of a sand
889 dune before and after the establishment of semi-buried straw checkerboard
890 barriers. *Aeolian Res* 20:59–70
- 891 Zhang D, Yang X, Rozier O, Narteau C (2014) Mean sediment residence time in
892 barchan dunes. *Journal of Geophysical Research: Earth Surface* 119(3):451–
893 463
- 894 Zilker DP, Hanratty TJ (1979) Influence of the amplitude of a solid wavy wall
895 on a turbulent flow. part 2. separated flows. *J Fluid Mech* 90:257–271
- 896 Zilker DP, Cook GW, Hanratty TJ (1977) Influence of the amplitude of a solid
897 wavy wall on a turbulent flow. part 1. non-separated flows. *J Fluid Mech*
898 82:29–51

899 **Local wind regime induced by giant linear dunes**
 900 — Supplementary Material —

901 **C. Gadal* · P. Delorme · C. Narteau · G.F.S. Wiggs · M. Baddock ·**
 902 **J.M. Nield · P. Claudin**

903

904 * Institut de Mécanique des Fluides de Toulouse, Université de Toulouse Paul
 905 Sabatier, CNRS, Toulouse INP-ENSEEIHT, Toulouse, France.

906 cyril.gadal@imft.fr

907 **1. Shear velocity and calibration of the hydrodynamical roughness**

908 As the regionally predicted and locally measured velocities are available at
 909 different heights, we can not compare them directly. We therefore convert
 910 all velocities into shear velocities u_* , characteristic the turbulent logarithmic
 911 velocity profile (Spalding 1961; Stull 1988):

$$\frac{u(z)}{u_*} = \frac{1}{\kappa} \ln \left(\frac{z}{z_0} \right), \quad (15)$$

912 where z is the vertical coordinate, $\kappa = 0.4$ the von Kármán constant and z_0 the
 913 hydrodynamic roughness. Note that, strickly speaking, this logarithmic profile
 914 is valid for a neutrally stratified ABL only. Vertical density gradients occurring
 915 in other conditions may thus induce large discrepancies (Monin and Obukhov
 916 1954; Garratt 1994; Dyer 1974). However, as our wind measurements are in
 917 the flow region close enough to the surface, where these effects are negligible,
 918 this logarithmic wind profile remains a fairly good approximation in all conditons
 919 (Gunn et al. 2021). Several measurements of hydrodynamic roughnesses
 920 are available (Raupach 1992; Bauer et al. 1992; Brown et al. 2008; Nield et al.
 921 2014). In the absence of sediment transport, it is governed by the geometric
 922 features of the bed (Flack and Schultz 2010; Pelletier and Field 2016). When
 923 aeolian saltation occurs, it is rather controlled by the altitude of Bagnold's
 924 focal point (Durán et al. 2011; Valance et al. 2015), which depends on the
 925 wind velocity and grain properties (Sherman and Farrell 2008; Zhang et al.
 926 2016; Field and Pelletier 2018). Whether associated with geometric features
 927 or with sediment transport, its typical order of magnitude is the millimetre
 928 scale on sandy surfaces.

929 We do not have precise velocity vertical profiles to be able to deduce an
 930 accurate value of z_0 in the various environments of the meteorological stations
 931 (vegetated, arid, sandy). Our approach is to rather select the hydrodynamic
 932 roughness which allows for the best possible matching between the regionally
 933 predicted and locally measured winds, i.e. minimising the relative difference δ
 934 between the wind vectors of both datasets:

$$\delta = \frac{\sqrt{\langle \| \mathbf{u}_{*,\text{era}} - \mathbf{u}_{*,\text{station}} \|^2 \rangle}}{\sqrt{\langle \| \mathbf{u}_{*,\text{era}} \|^2 \rangle \langle \| \mathbf{u}_{*,\text{station}} \|^2 \rangle}}, \quad (16)$$

where $\langle \cdot \rangle$ denotes time average. This parameter is computed for values of z_0 in ERA5-Land analysis ranging from 10^{-5} m to 10^{-2} m for the four different stations. Note that for the North Sand Sea and South Sand Sea stations, where the giant dunes feedback presumably affect the wind, we take into account the non-deflected winds only in the calculation of δ (with a 15° tolerance).

As shown in Online Resource Fig. S3, the minimum values of δ in the space $(z_0^{\text{ERA5Land}}, z_0^{\text{local}})$ form a line. We thus set the roughness in the ERA5-Land analysis to the typical value $z_0 = 10^{-3}$ m, and deduce the corresponding ones for the local stations. It leads to 2.7, 0.8, 0.1 and 0.5 mm for the Etosha West, North Sand Sea, Huab and South Sand Sea stations, respectively. Importantly, this approach somewhat impacts the calculation of the shear velocities, but not that of the wind directions. As such, most of our conclusions are independent of such a choice. However, it may affect the magnitude of the wind velocity attenuation/amplification in flow confinement situations.

2. Computation of the ABL characteristics

The estimation of the non-dimensional numbers associated with the ABL requires the computation of representative meteorological quantities. In arid areas, the vertical structure of the atmosphere can be approximated by a well mixed convective boundary layer of height H , topped by the stratified free atmosphere (Stull 1988; Shao 2008). In this context, one usually introduces the virtual potential temperature T_{vp} , which is a constant T_0 inside the boundary layer, and increases linearly in the FA (Online Resource Fig. S8a):

$$T_{\text{vp}}(z) = \begin{cases} T_0 & \text{for } z \leq H, \\ T_0 \left(1 + \frac{\Delta T_{\text{vp}}}{T_0} + \frac{N^2}{g}(z - H) \right) & \text{for } z \geq H, \end{cases} \quad (17)$$

where ΔT_{vp} is the temperature discontinuity at the capping layer and $N = \sqrt{g\partial_z T_{\text{vp}}/T_0}$ is the Brunt-Väisälä frequency, characteristic of the stratification. Note that, under the usual Boussinesq approximation, temperature and air density variations are simply related by $\delta T_{\text{vp}}/T_0 \simeq -\delta\rho/\rho_0$ (see Online Resource of Andreotti et al. (2009)), so that N can equivalently be defined from the density gradient as next to (1).

The ERA5 dataset provides vertical profiles of the geopotential ϕ , the actual temperature T and the specific humidity η at given pressure levels P . The vertical coordinate is then calculated as:

$$z = \frac{\phi R_t}{g R_t - \phi}, \quad (18)$$

where $R_t = 6371229$ m is the reference Earth radius and $g = 9.81$ m s $^{-2}$ is the gravitational acceleration. One also computes the virtual potential temperature as:

$$T_{\text{vp}} = T \left[1 + \left(\frac{M_d}{M_w} - 1 \right) \eta \right] \left(\frac{P_0}{P} \right)^{R/C_p}, \quad (19)$$

where $P_0 = 10^5$ Pa is the standard pressure, $R = 8.31$ J/K is the ideal gas constant, $C_p \simeq 29.1$ J/K is the air molar heat capacity, and $M_w = 0.018$ kg/Mol and $M_d = 0.029$ kg/Mol are the molecular masses of water and dry air respectively. The specific humidity is related to the vapour pressure p_w as

$$\eta = \frac{\frac{M_w}{M_d} p_w}{p - \left(1 - \frac{M_w}{M_d}\right) p_w}. \quad (20)$$

The ERA5 dataset also provides an estimate of the ABL depth H , based on the behaviour of the Richardson vertical profile. This dimensionless number is defined as the ratio of buoyancy and flow shear terms, and can be expressed as $\text{Ri} = N^2 / (\partial_z u)^2$. It vanishes in the lower well-mixed layer where T_{vp} is constant, and increases in the stratified FA. Following the method and calibration of Vogezezang and Holtlag (1996); Seidel et al. (2012), the value $\text{Ri}(z) \simeq 0.25$ has been shown to be a good empirical criterion to give $z \simeq H$ within a precision varying from 50% for the shallower ABL (e.g. at night) to 20% for situations of stronger convection.

Examples of vertical virtual potential temperature profiles deduced from ERA5 are shown in Online Resource Fig. S8a. For each of them, an average temperature is computed below the ABL depth ($z < H$), and a linear function is fitted above, allowing us to extract the temperature jump ΔT_{vp} . Importantly, some profiles display a vertical structure that cannot be approximated by the simple form (17) used here (Online Resource Fig. S8b). In practice, we removed from the analysis all of those leading to the unphysical case $\Delta T_{vp} < 0$. We have noticed that these ‘ill-processed’ profiles dominantly occur in winter and are evenly spread across the hours of the day. Importantly, they represent $\simeq 12\%$ of the data only (Online Resource Fig. S8c,d), and we are thus confident that this data treatment does not affect our conclusions.

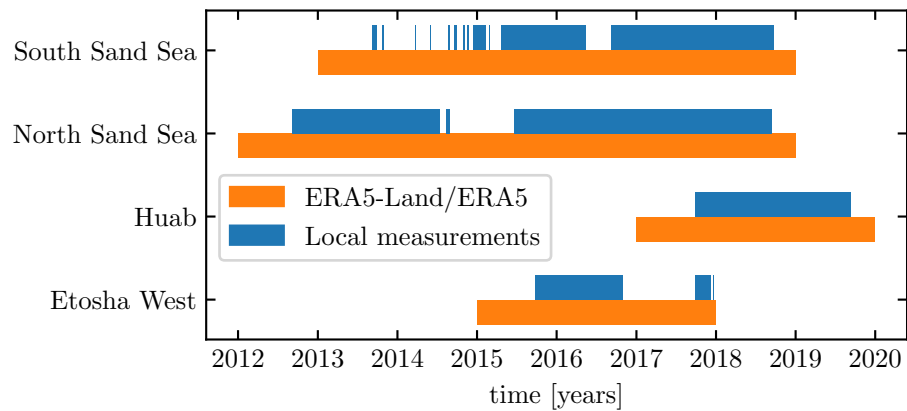


Fig. S1 Gantt chart representing the valid time steps for the two data sets, for all stations.

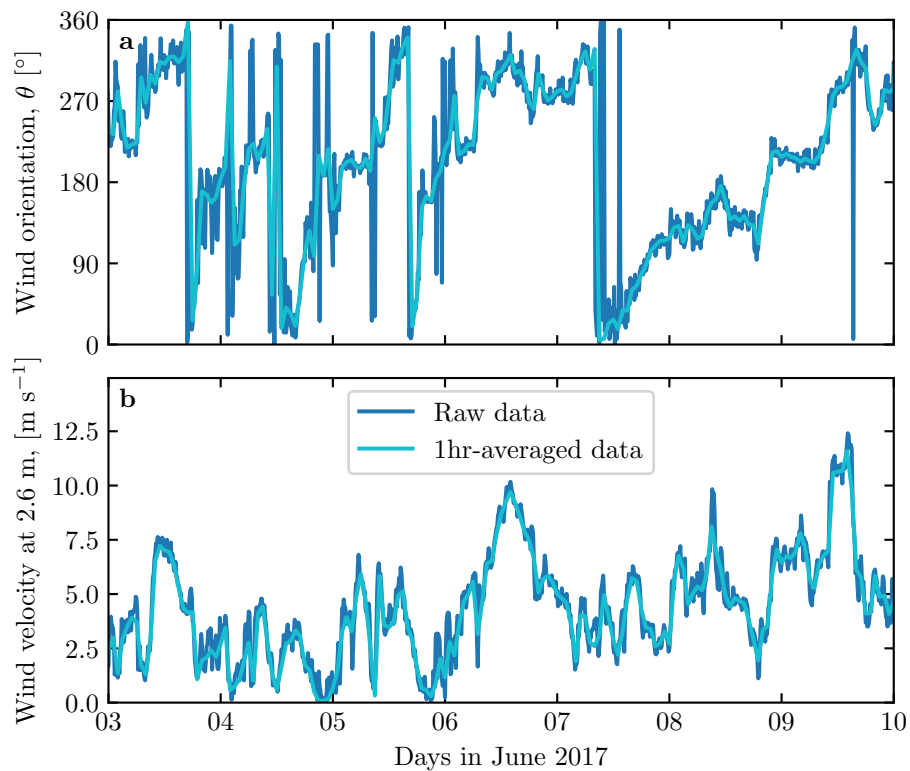


Fig. S2 Local wind measurements: comparison between raw (blue) and hourly-averaged (light blue) data from South Sand Sea station. **a:** wind direction. **b:** wind velocity at height 2.6 m.

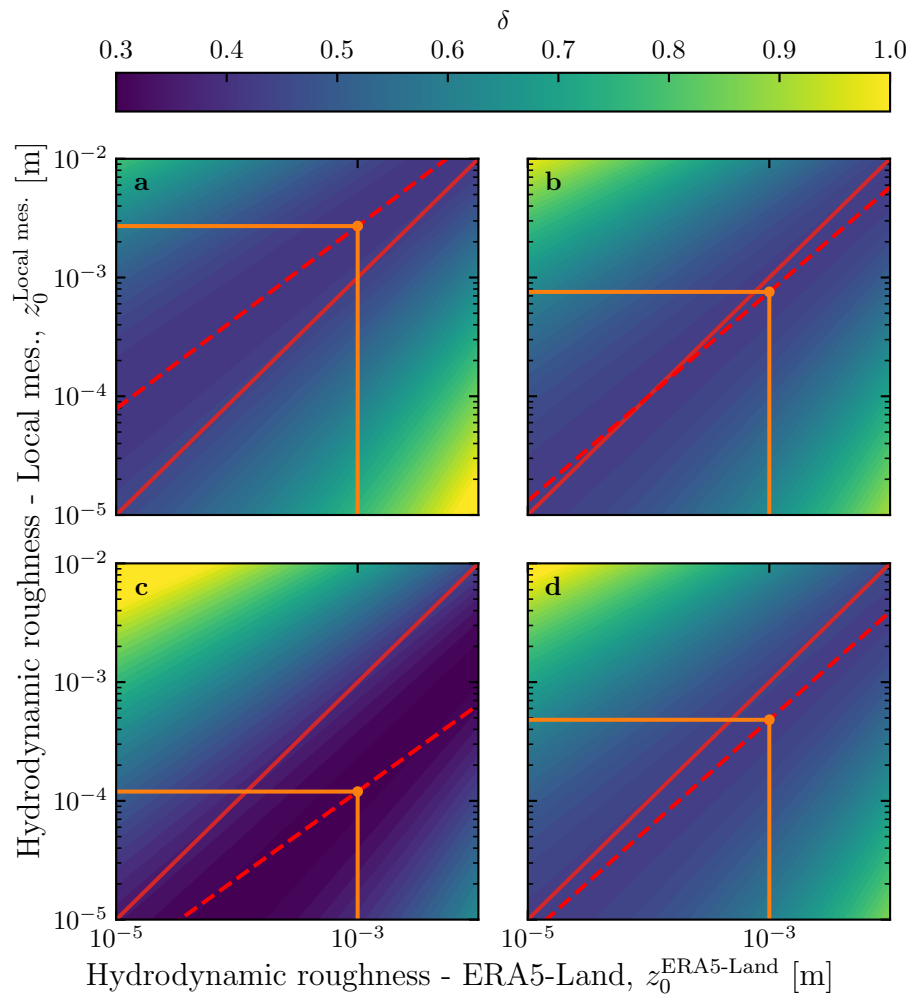


Fig. S3 Calibration of hydrodynamic roughness. The parameter δ (16) quantifying the difference between local and predicted winds is shown in color scale as a function of the hydrodynamic roughnesses chosen for the ERA5-Land and for local winds, for the (a) Etosha West, (b) North Sand Sea, (c) Huab and (d) South Sand Sea stations. The red dashed and plain lines shows the minima of δ and the identity line, respectively. The orange lines and dots highlight the chosen hydrodynamic roughnesses for the local winds deduced from setting $z_0^{\text{ERA5-Land}} = 1 \text{ mm}$.

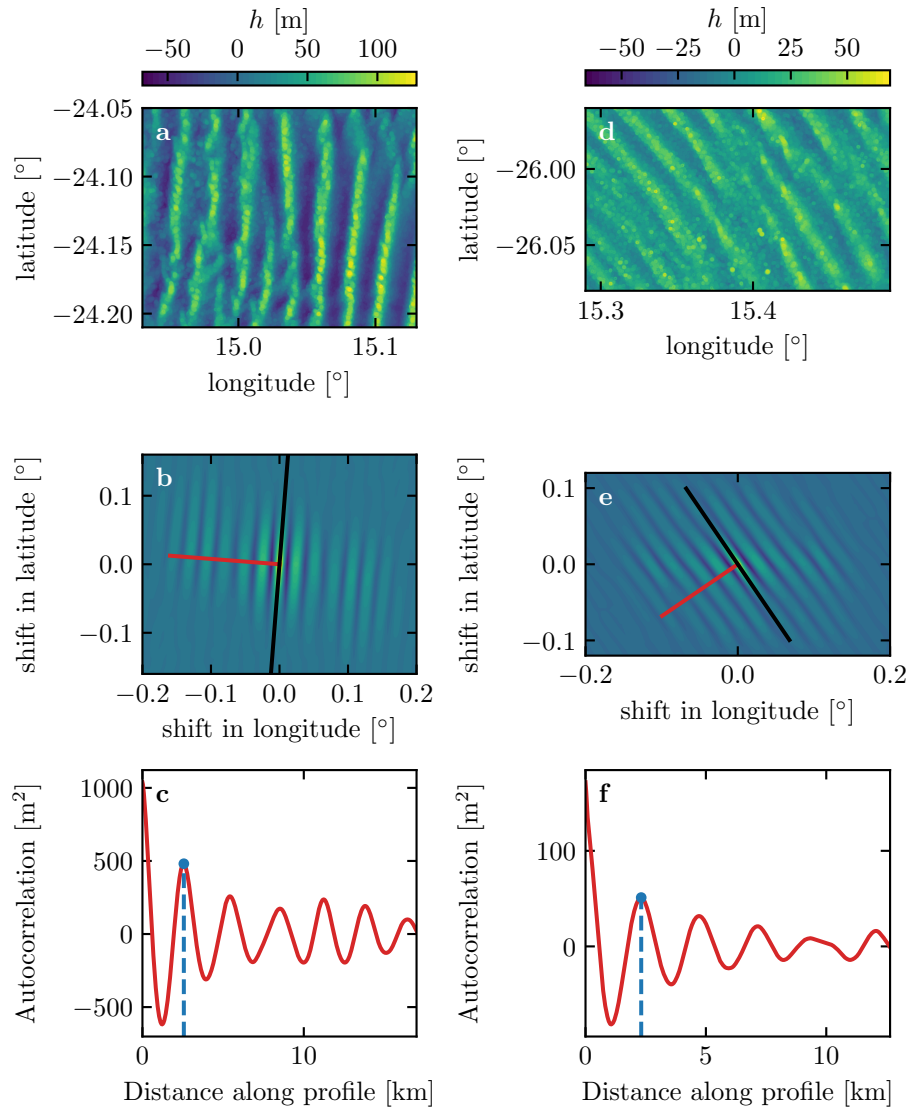


Fig. S4 Analysis of the DEMs of the North Sand Sea (left column – panels **a**, **b**, **c**) and South Sand Sea (right column – panels **d**, **e**, **f**) stations. **a–d**: Bed elevation detrended by a fitted second order polynomial base-line. **b–e**: Autocorrelation matrix shown in color scale. The black line shows the detected dune orientation, and the red line represents the autocorrelation profile along which the dune wavelength is calculated, displayed in **c–f**. The blue lines and dots show the first peak of the autocorrelation profile, whose abscissa gives the characteristic wavelength of the dune pattern.

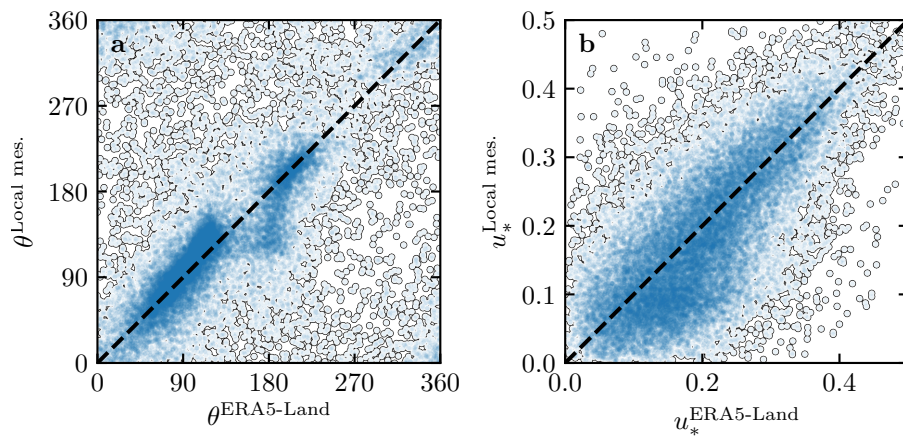


Fig. S5 Statistical comparison of the wind orientation (a) and velocity (b) between the ERA5-Land dataset and the local measurements for the Huab and Etosha West stations. Data point clustering around identity lines (dashed and black) provide evidence for agreement of the two sets.

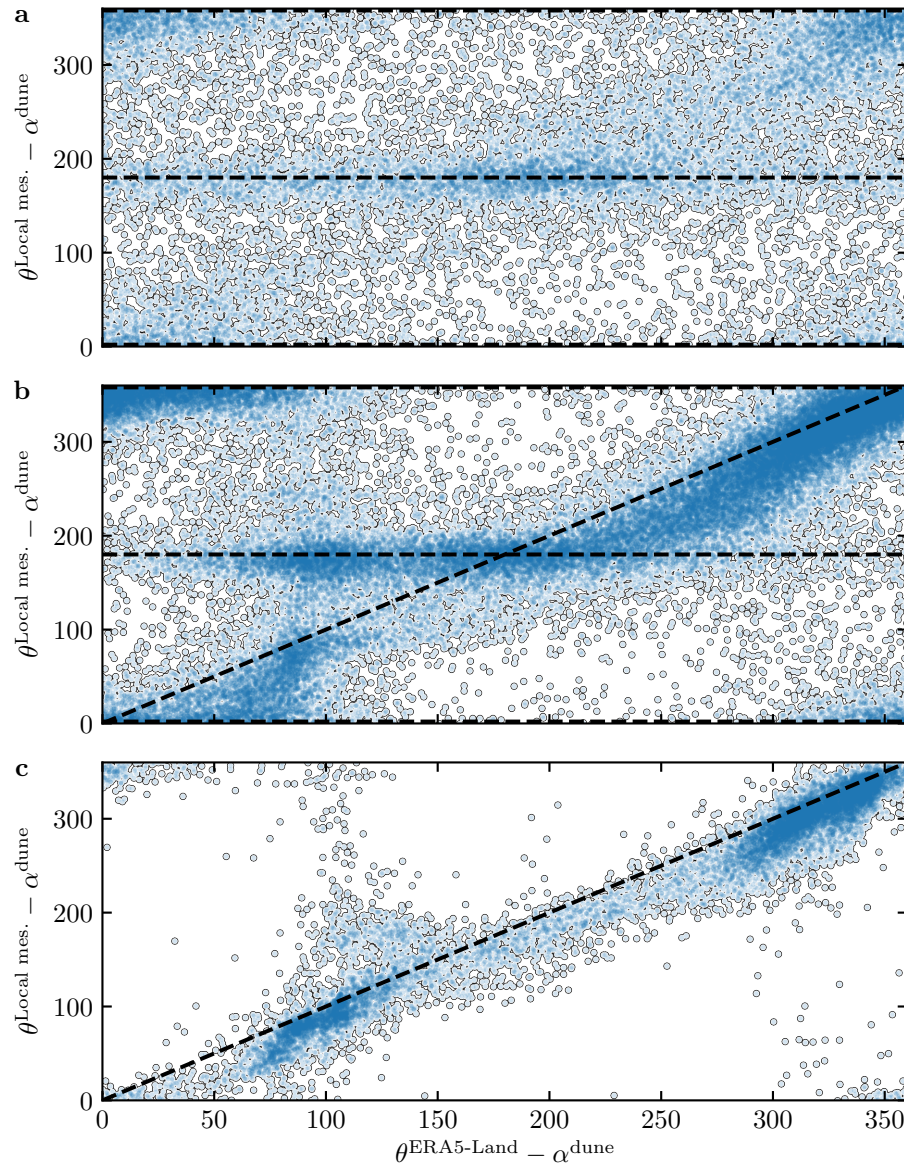


Fig. S6 Statistical comparison of the wind orientation between the ERA5-Land dataset and the local measurements for the South Sand Sea and North Sand Sea stations, for different velocity ranges. **a:** $u_*^{\text{ERA5-Land}} < 0.1 \text{ m s}^{-1}$. **b:** $0.1 < u_*^{\text{ERA5-Land}} \leq 0.25 \text{ m s}^{-1}$. **c:** $u_*^{\text{ERA5-Land}} \geq 0.25 \text{ m s}^{-1}$. The measured dune orientations are subtracted to the wind orientation, which allows us to plot both stations on the same graph. Black dashed lines indicate locally measured orientations aligned with the dune crests (here 0°, 180° and 360° – panels **a, b**), as well as the identity lines (panels **b, c**).

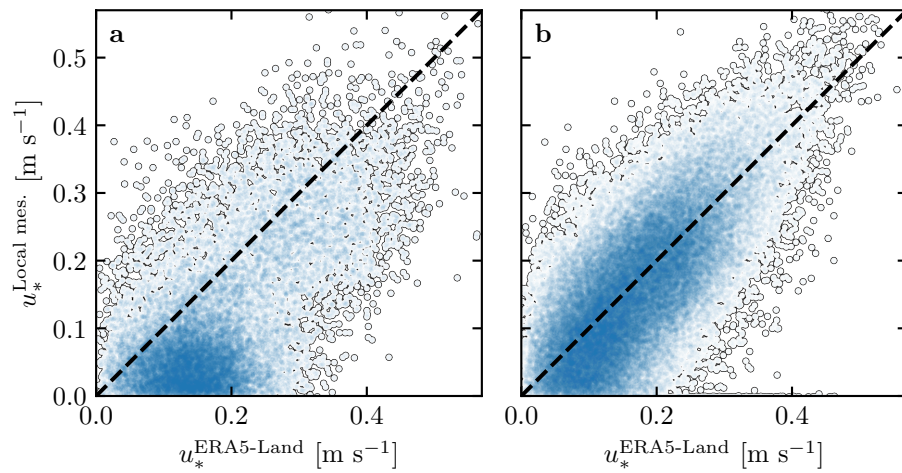


Fig. S7 Statistical comparison of the wind velocity between the ERA5-Land dataset and the local measurements for the South Sand Sea and North Sand Sea stations. **a:** Nocturnal summer easterly wind. **b:** Diurnal southerly wind. Black dashed lines are identity lines. The angle ranges used to select diurnal and nocturnal summer winds are the same as those in Figs. 4 and Figs. 6 of the main article.

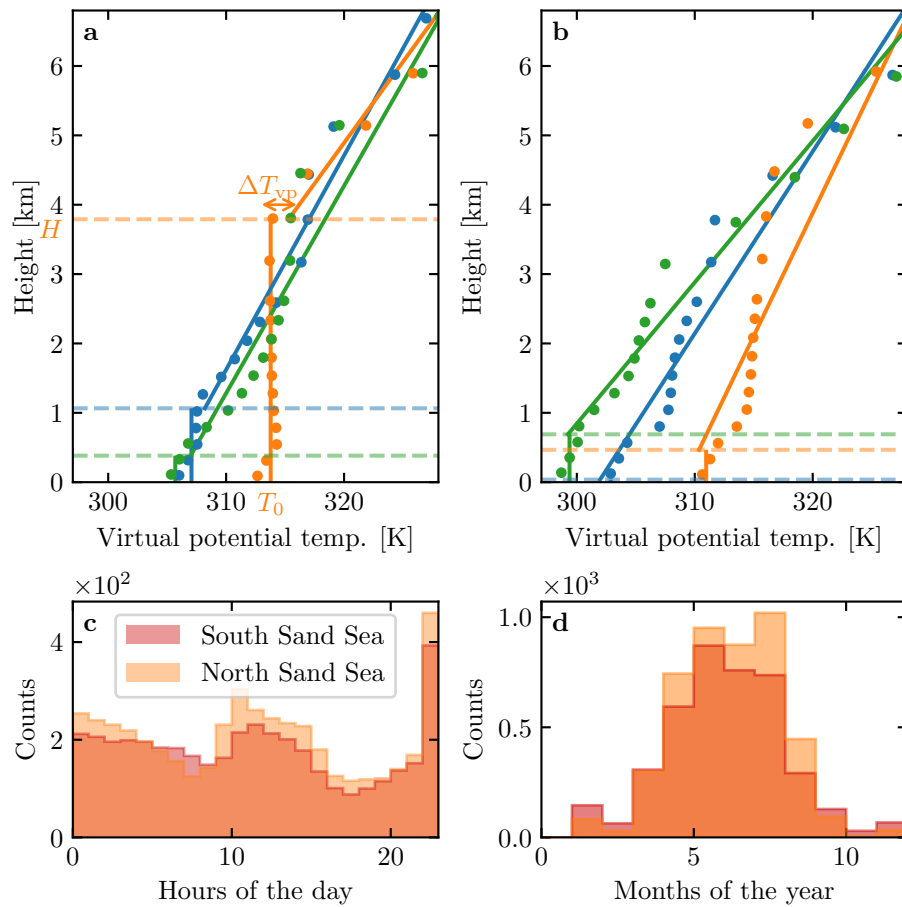


Fig. S8 **a:** Vertical profiles of the virtual potential temperature at three different times (blue: 29/11/2012 - 11.00 UTC, orange: 21/03/2017 - 12.00 UTC, green: 21/03/2017 - 20.00 UTC) at the South Sand Sea station. Dots: data from the ERA5 reanalysis. Dashed lines: boundary layer height given by the ERA5 reanalysis. Plain lines: vertical (ABL) and linear (FA) fits to estimate the quantities displayed in Online Resource Fig. S9. **b:** Examples of ill-processed vertical profiles at three different times (blue: 2/12/2013 - 23.00 UTC, orange: 20/03/2017 - 00.00 UTC, green: 14/07/2017 - 14.00 UTC) at the South Sand Sea station. Distribution of ill-processed vertical profiles at South (orange) and North (light orange) Sand Sea station: hourly **(c)** and monthly **(d)** counts.

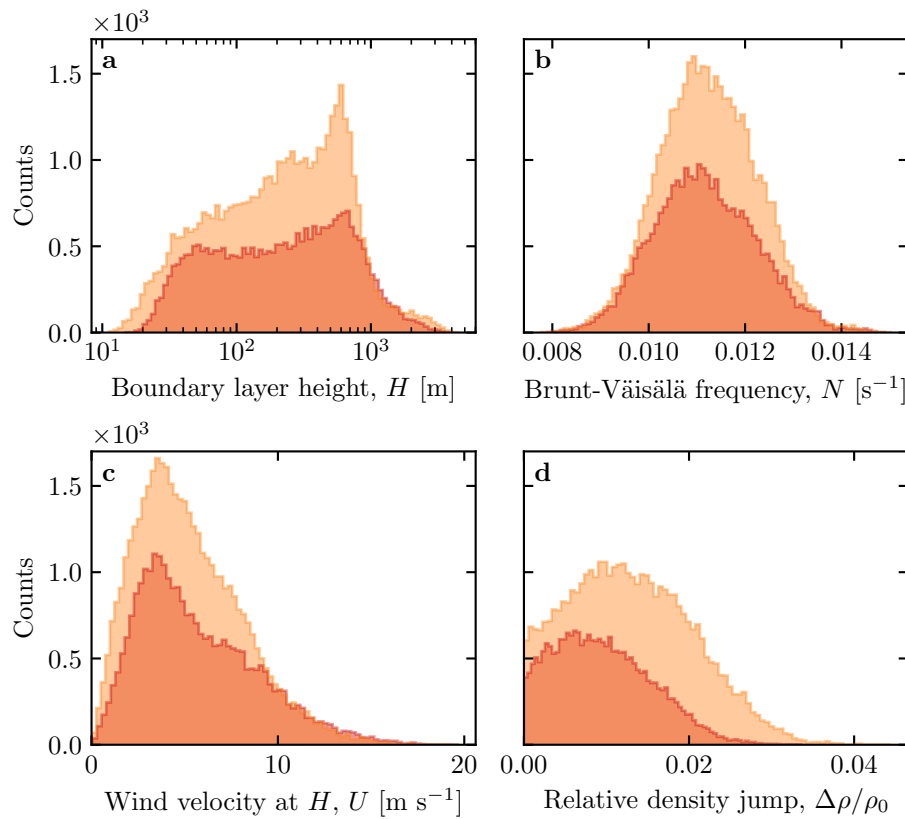


Fig. S9 Distributions of the meteorological parameters resulting from the processing of the ERA5-Land data for the South Sand Sea (orange) and the North Sand Sea (light orange) stations.

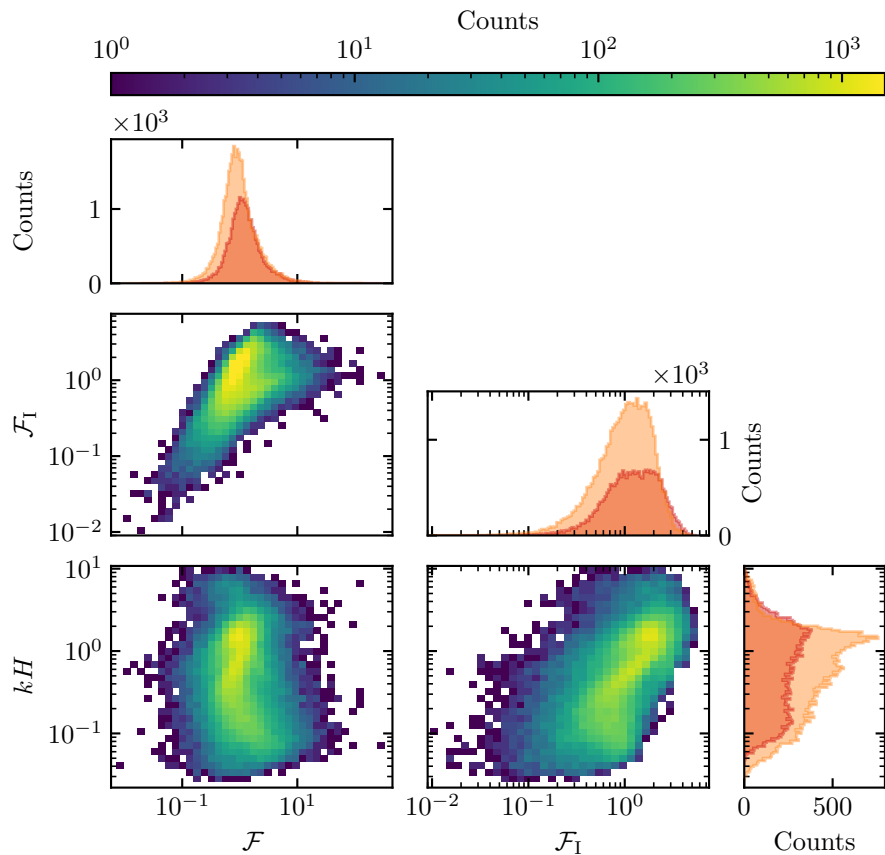


Fig. S10 Non-dimensional parameters distributions. For the marginal distributions, the light orange corresponds to the South Sand Sea station, and the orange to the North Sand Sea station.

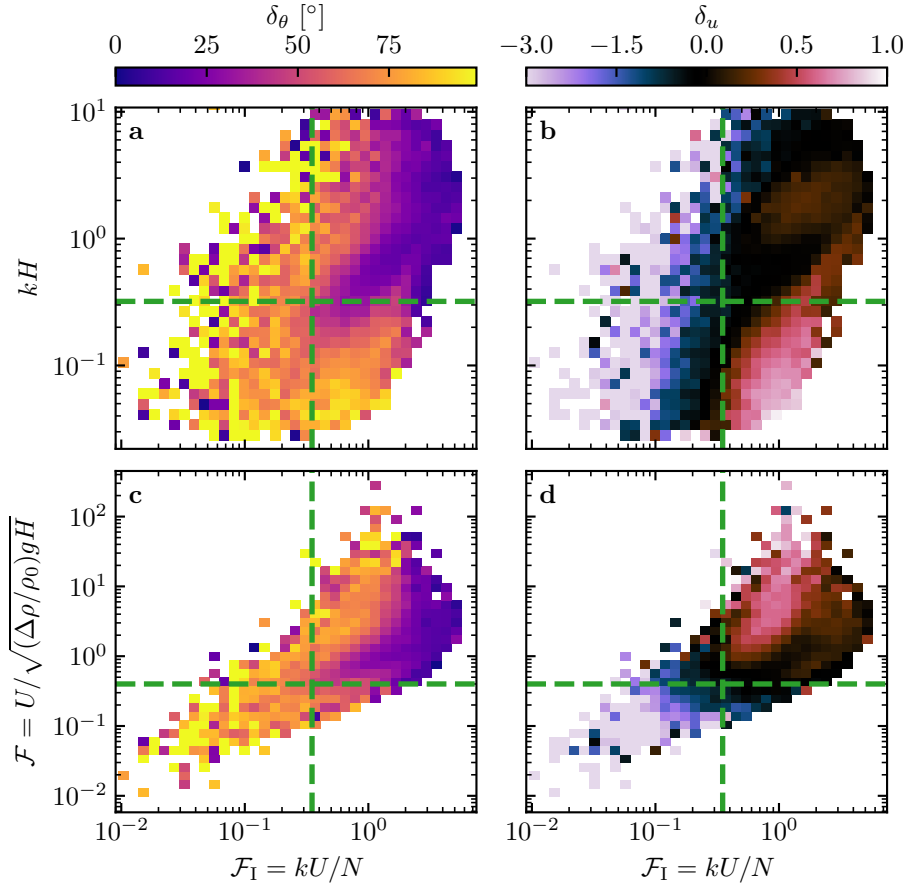


Fig. S11 Regime diagrams of the wind deviation δ_θ and relative attenuation/amplification δ_u in the spaces (\mathcal{F}_I, kH) and $(\mathcal{F}_I, \mathcal{F})$, containing the data from both the North Sand Sea and South Sand Sea stations. Green dashed lines empirically delimit the different regimes. The point density in each bin of the diagrams is shown in Online Resource Fig. S10 – 95% of the data occur in the range $-1 < \delta u < 1$. The similar regime diagrams in the space (\mathcal{F}, kH) are shown in Fig. 8.

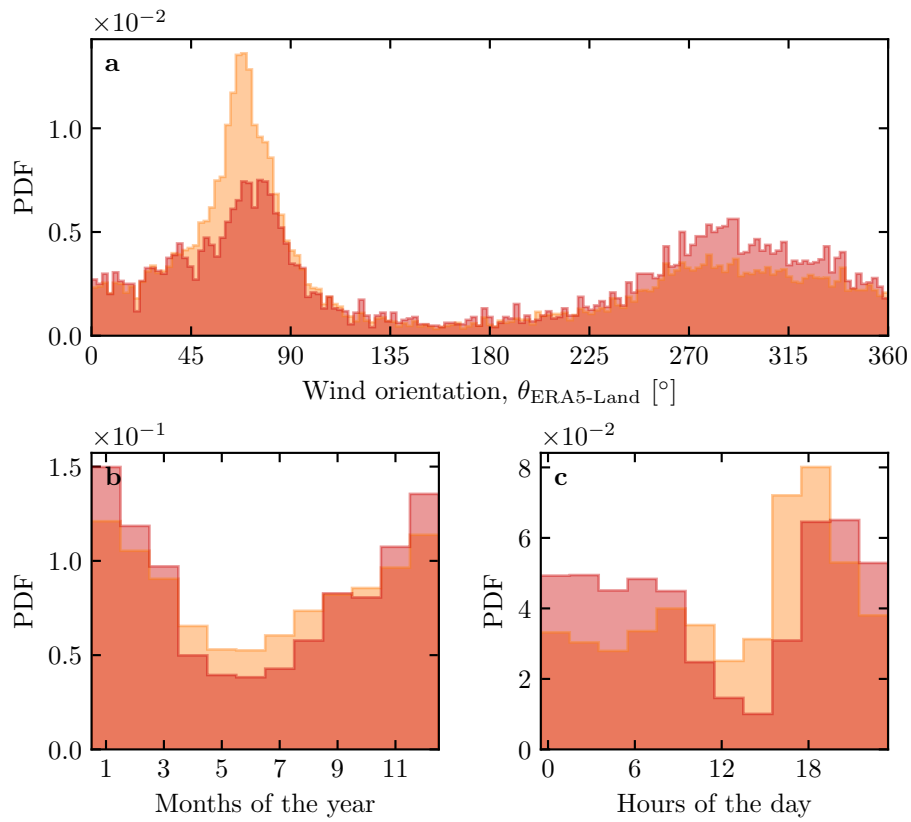


Fig. S12 Normalized distributions of amplified velocities for the North Sea (light orange: $\delta_u < 0$, orange: $\delta_u < -0.5$). **a:** Angular distributions. **b:** Monthly distributions. **c:** Hourly distributions.

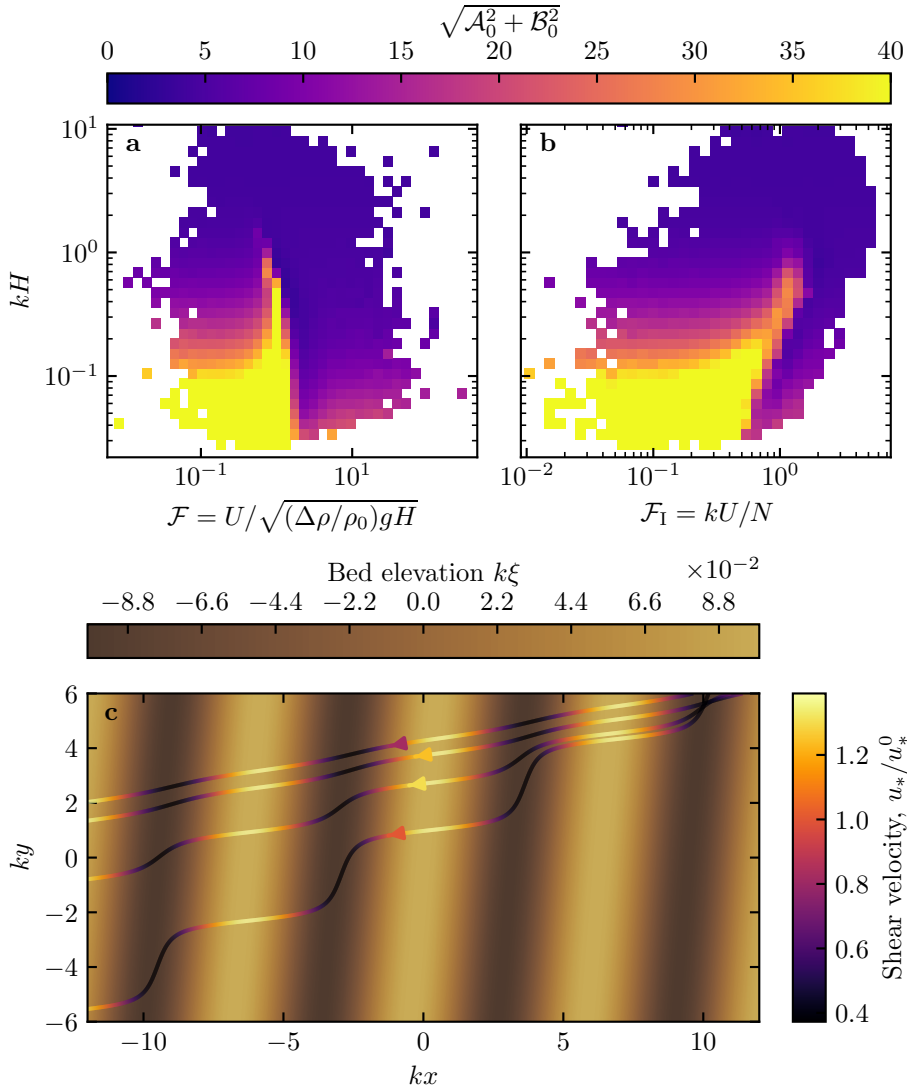


Fig. S13 Computation of the flow disturbance with the linear model of Andreotti et al. (2009). **a–b:** Magnitude of the hydrodynamic coefficients A_0 and B_0 , calculated from the time series of the non-dimensional numbers corresponding to the ERA5-Land wind data and ERA5 data on vertical pressure levels. **c** Shear velocity streamlines over sinusoidal ridges of amplitude $k\xi_0 = 0.1$ and for increasing values of $\sqrt{A_0^2 + B_0^2}$. From the upper to the lower streamline, values of $(kH, \mathcal{F}, \mathcal{F}_I, A_0, B_0, \sqrt{A_0^2 + B_0^2})$ are $(1.9, 0.6, 1.5, 3.4, 1.0, 3.5)$, $(1.5, 0.3, 0.4, 4.8, 1.4, 5.0)$, $(0.1, 3.5, 1.0, 8.6, 0.1, 8.6)$, $(0.5, 0.05, 0.04, 9.6, 2.5, 9.9)$.

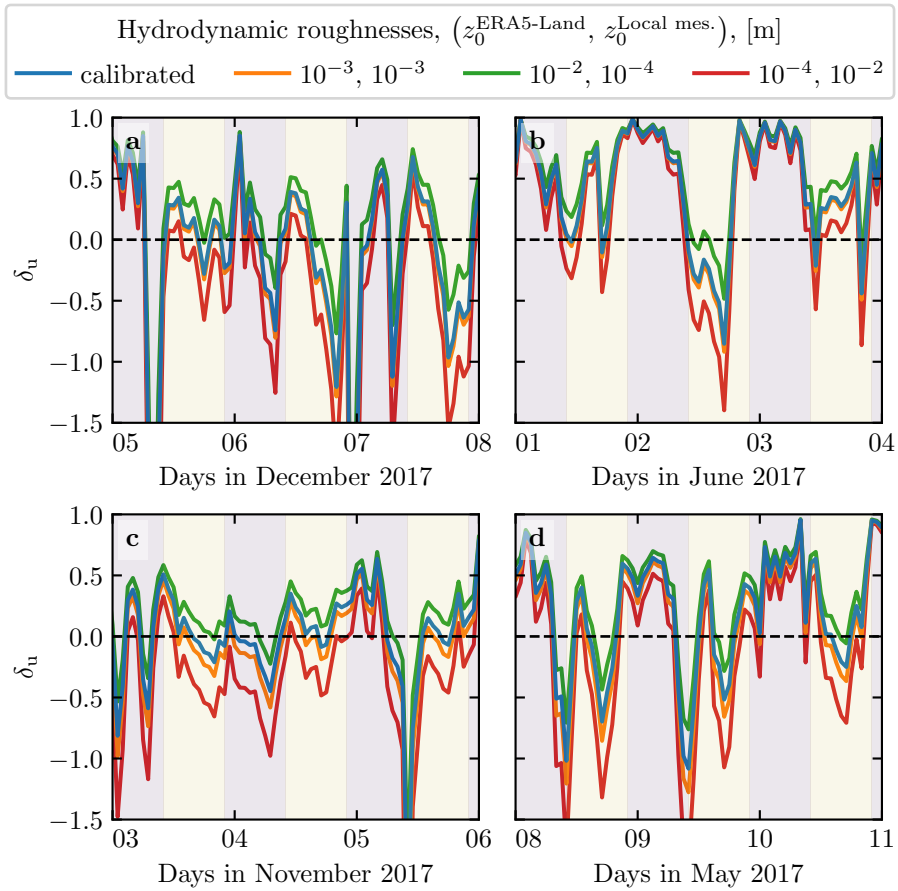


Fig. S14 Time series of the relative velocity disturbance δ_u corresponding to Fig. 5, for different values of the hydrodynamic roughnesses. **a:** North Sand Sea – summer, **b:** North Sand Sea – winter, **d:** South Sand Sea – summer, **e:** South Sand Sea – winter. Note that δ_θ is independent of the choice of $z_0^{\text{ERA5-Land}}$ and $z_0^{\text{Local mes.}}$.